STUDIA UNIVERSITATIS
BABEŞ-BOLYAI

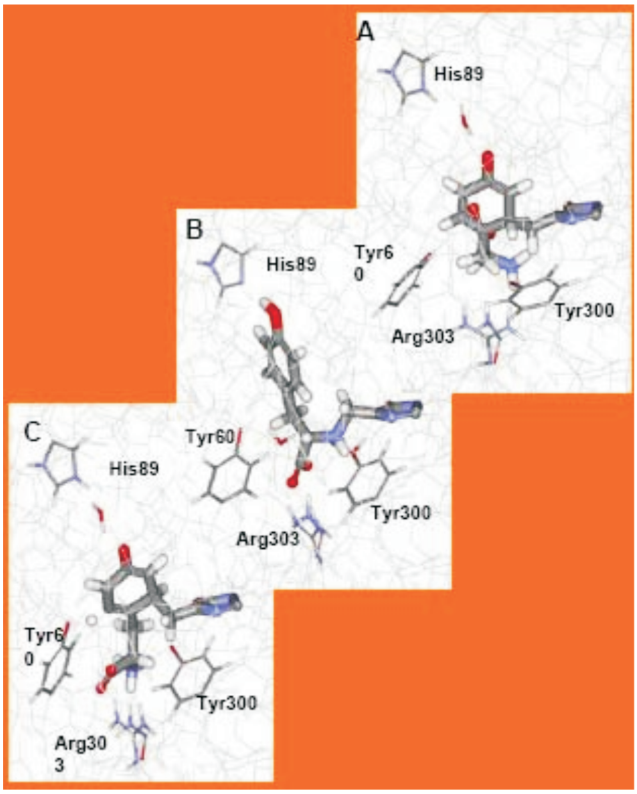
A
His89
Tyr6
0
Tyr300
Arg303
B
His89
Tyr60
Tyr300
Arg303
C
His89
Tyr6
0
Tyr300
Arg30
3

CHEMIA

2/2008

ANUL LIII 2008

S T U D I A

UNIVERSITATIS BABEŞ-BOLYAI

CHEMIA

2

Desktop Editing Office: 51^{ST} B.P. Hasdeu Street, Cluj-Napoca, Romania, Phone + 40 264-405352

CUPRINS – CONTENT – SOMMAIRE – INHALT

P. G. MEZEY, CORNELIA MAJDIC, Measures of Shape Similarity of Electron Density Clouds in Molecular Modeling 7

LÁSZLÓ POPPE, SAROLTA PILBÁK, CSABA PAIZS, JÁNOS RÉTEY, Mechanistic aspects and biocatalytic implications of the MIO-containing ammonia-lyase / aminomutase family 15

C.J.R. ILLIGWORTH, P.J. WINN, G.G. FERENCZY, C.A. REYNOLDS, Progress in Modelling Electrostatics and Polarization through Effective Multipoles and Induced Charges 21

R. BRUCE KING, HENRY F. SCHAEFER, YAOMING XIE, QIAN-SHU LI, XIUHUI ZHANG, HONGYAN WANG, Unsaturation in Binuclear First Row Cyclopentadienylmetal Carbonyls as Studied by Density Functional Theory... 29

BEÁTA PELES-LEMLI, JÁNOS PELES-LEMLI, LÁSZLÓ KOLLÁR, GÉZA NAGY, SÁNDOR KUNSÁGI-MÁTÉ, Temperature-Independent Longitudinal Waves Obtained on Carbon Nanotubes with Special Emphasis on the Tubular Ion-Transport 37

BENJAMIN PARENT, ALEXANDRU TANTAR, NOUREDINE MELAB, EL-GHAZALI TALBI, DRAGOS HORVATH, Grid-Based Conformational Sampling 43

MIRCEA V. DIUDEA, Basic Tessellations in Nanostructures 49

RADU SILAGHI-DUMITRESCU, MATEI-MARIA UȚĂ, Nitrite Linkage Isomerism in Bioinorganic Chemistry – A Case for Mechanistic Promiscuity 61

AMALIA-LAURA SEFF, SAROLTA PILBÁK, LÁSZLÓ POPPE, Ligand Docking and Systematic Conformational Analysis in Loop Modified Parsley Phenylalanine Ammonia-Lyase Structure 67

MIHAI V. PUTZ, ANA-MARIA PUTZ (LACRĂMĂ), Spectral-SAR: Old Wine in New Bottle 73

IOAN SILAGHI-DUMITRESCU, BRUCE KING, Germanium Cluster Polyhedra 83

Studia Universitatis Babes-Bolyai Chemia has been selected for coverage in Thomson Reuters products and custom information services. Beginning with V. 53 (1) 2008, this publication will be indexed and abstracted in the following:

- Science Citation Index Expanded (also known as SciSearch®)
- Chemistry Citation Index®
- Journal Citation Reports/Science Edition

This issue contains extended abstracts of a part of the talks given at THE SECOUND MOLECULAR MODELING IN CHEMISTRY AND BIOCHEMISTRY CONFERENCE (MOLMOD) (July 5-7, 2007) organized at the Arcalia Castle of Babeş-Bolyai University.

We thank again all participants for their valuable contributions and thank particularly those who agreed to publish their abstracts in this journal.

Cluj-Napoca, July 31, 2008

On behalf of the organizers of the conference
Paul MEZEY,
Ioan SILAGHI-DUMITRESCU

STUDIA UNIVERSITATIS BABEŞ-BOLYAI, CHEMIA, LIII, 2, 2008

MEASURES OF SHAPE SIMILARITY OF ELECTRON DENSITY CLOUDS IN MOLECULAR MODELING

PAUL G. MEZEY[a,b,*], CORNELIA MAJDIK[c]

ABSTRACT. Shape similarity measures for molecular electron densities may serve many purposes, one important application of such measures is in QSAR, where precise electron density comparisons provide high levels of correlations with various biochemical activities. Some shape similarity measures are "strictly shape-based", in the sense that they ignore all size information, and they can be considered "pure" shape similarity measures. In this contribution it is argued that shape similarity measures which retain some size information are likely to be better suited for some molecular applications, as a consequence of the relatively narrow range of the typical bond lengths, the typical sizes of functional groups, and the limited, but non-negligible local size variations of the associated electron density clouds due to the influence of their local surroundings.

INTRODUCTION

Similarity in chemistry plays a fundamental role; one may claim that the original understanding of most laws of chemistry has been based on the recognition of similarities between seemingly different molecules or phenomena. In searching for the explanation of those similarities, new theories and new laws have been discovered, hence similarity is fundamental in the development of chemistry, and in general, all sciences.

In recent years there has been a considerable amount of scientific work devoted to molecular similarity; for some of the main directions the reader may consult references [1-10]. In particular, QSAR approaches and drug design [11-14] have provided strong motivation to place similarity analysis on a strong foundation.

[a,*] *Scientific Modeling and Simulation Laboratory (SMSL), Department of Chemistry and Department of Physics and Physical Oceanography, Memorial University of Newfoundland, 283 Prince Philip Drive, St. John's, NL A1B 3X7, Canada, paul.mezey@gmail.com*

[b] *Institute for Advanced Study, Collegium Budapest, Szentháromság utca 2, 1014 Budapest, Hungary*

[c] *Babes-Bolyai University, Faculty of Chemistry and Chemical Engineering, Cluj-Napoca, 1, Kogalniceanu, RO-400084, Romania*

We shall focus on a particular, intuitively rather straightforward shape similarity measure, the so-called Scaling-Nesting Similarity Measure, SNSM, where the separation of shape and size features are especially clear [15,16]; this similarity measure has also provided motivation for some of the alternative, quantum chemical approaches [17].

SCALING-NESTING SIMILARITY MEASURES WITH AND WITHOUT PRE-SCALING

The main idea of the scaling-nesting similarity measure is very simple. If one restricts the analysis to objects of the same size, for example, to objects of the same volume or to planar objects of the same area, then if two objects A and B have exactly the same shape, then A fits within B and B fits within A perfectly. If they have different shapes, then each objects must be reduced in size, in order to fit within the other, and the maximal scaling factor that already allows one to fit within the other provides a numerical characterization of the difference in their shapes. This idea is illustrated by the two planar objects A and B in Figure 1.

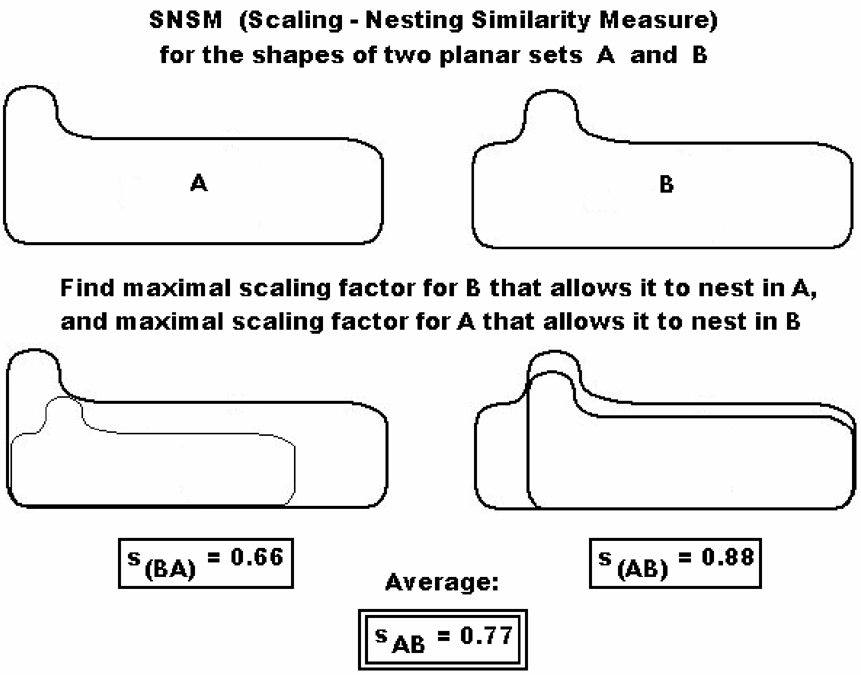
SNSM (Scaling - Nesting Similarity Measure)
for the shapes of two planar sets A and B
A
B
Find maximal scaling factor for B that allows it to nest in A,
and maximal scaling factor for A that allows it to nest in B
$s_{(BA)} = 0.66$
Average:
$s_{(AB)} = 0.88$
$s_{AB} = 0.77$

Figure 1. The Scaling-Nesting Similarity Measure applied to two planar objects A and B of the same area (same "size")

Usually, the two objects A and B require different scaling factors, hence a similarity measure based on such scaling initially provides only an asymmetric similarity measure, also called "Semi-Similarity Measure" [15]. Such asymmetric similarity measures may serve a useful purpose, when similarity may be interpreted differently from A to B than from B to A, for example, if similarity between languages of two populations of different mother tongues are analyzed in terms of the percentage of one population understanding the language of the other population, these percentages are often different, as it is the case for Spanish and Portuguese. However, in most cases one may prefer a measure that is symmetric, providing the same similarity value independently of the ordering of the objects of study. The simplest such measure is the average of the two numerical values of such asymmetric measures; evidently, the average must always be symmetric.

We denote the maximum scaling factor that allows A to fit within B by $s_{(A,B)}$, similarly, the maximum scaling factor that allows B to fit within A is denoted by $s_{(B,A)}$, and the average of the two factors by s_{AB},

$$s_{AB} = (s_{(A,B)} + s_{(B,A)}) / 2 \tag{1}$$

a function evidently symmetric for the interchange of A and B.

We can often formulate property correlations easier in terms if dissimilarity than in terms of similarity. The associated Scaling-Nesting Dissimilarity Measure can be defined as

$$S_{AB} = 1- s_{AB} = 1 - (s_{(A,B)} + s_{(B,A))} / 2 \tag{2}$$

Evidently, this Scaling-Nesting Dissimilarity Measure S_{AB} is also symmetric for the interchange of A and B.

For this Scaling-Nesting Dissimilarity Measure, it is easy to prove an even stronger statement, not restricted to symmetry. In fact, the Scaling-Nesting Dissimilarity Measure is a proper metric, fulfilling all the general mathematical conditions for a "distance-like" function:

$$S_{AB} \geq 0, \qquad \text{(non-negativity)} \tag{3}$$

$$S_{AB} = 0 \text{ if and only if } A=B \qquad \text{(identity)} \tag{4}$$

$$S_{AB} = S_{BA} \qquad \text{(symmetry)} \tag{5}$$

$$S_{AC} \leq S_{AB} + S_{AB} \qquad \text{(triangle inequality)} \tag{6}$$

The first three conditions are trivially fulfilled, and the triangle inequality can also be verified [16]; a simple demonstration is given below.

The triangle inequality we want to prove, inequality (6), can be written explicitly in terms of the symmetric similarity measures as

$$1- s_{AC} \leq 1- s_{AB} + 1- s_{BC} \tag{7}$$

and in terms of the semi-similarity measures as

$$1 - (s_{(A,C)} + s_{(C,A))} / 2 \quad \leq 1 - (s_{(A,B)} + s_{(B,A))} / 2 + 1 - (s_{(B,C)} + s_{(C,B)} / 2 \tag{8}$$

that reduces to

$$s_{(A,B)} + s_{(B,C)} - s_{(A,C)} + s_{(C,B)} + s_{(B,A)} - s_{(C,A)} \leq 2 \; . \tag{9}$$

In order to prove inequality (9), let us first consider two ways of scaling A to fit within C: directly, with maximum scaling factor $s_{(A,C)}$, or in two steps, first scaling A to fit within B, then scaling B (with the scaled A included) to fit within C. Evidently, this second procedure will also result in A being scaled so it is included in C, however, this second process is less efficient, and the overall scaling factor for this process is the product of the two scaling factors, $s_{(A,B)}\, s_{(B,C)}$, where this product cannot exceed $s_{(A,C)}$, this latter being the maximum scaling factor. Consequently,

$$s_{(A,B)}\, s_{(B,C)} \leq s_{(A,C)} \tag{10}$$

We also realize that for the positive quantities bounded by 1,

$$0 \leq s_{(A,B)} \, , \; s_{(B,C)} \leq 1 \tag{11}$$

the inequality

$$0 \leq (s_{(A,B)} - 1) (s_{(B,C)} - 1) \tag{12}$$

must always hold, that gives

$$s_{(A,B)} + s_{(B,C)} - s_{(A,B)}\, s_{(B,C)} \leq 1 \tag{13}$$

Due to inequality (10), the product $s_{(A,B)}\, s_{(B,C)}$ cannot be greater than $s_{(A,C)}$, consequently, replacing the former with the latter in inequality (13) only strengthens this inequality, and

$$s_{(A,B)} + s_{(B,C)} - s_{(A,C)} \leq 1 \; . \tag{14}$$

Precisely the same way we obtain

$$s_{(C,B)} + s_{(B,A)} - s_{(C,A)} \leq 1 \; . \tag{15}$$

The sum of the two inequalities (14) and (15) then gives inequality (9), that proves the triangle inequality for the Scaling Nesting Dissimilarity Measure, and also completes the verification that it is indeed a metric.

This dissimilarity measure S_{AB} is a “pure” shape measure, as it is independent of size; in fact, for its application to objects of different size, a pre-scaling to a common size is needed, otherwise the scaling factors may take any values, independent of the actual shapes involved.

Whereas skipping pre-scaling to a common size may render some of the advantageous properties of the metric invalid, nevertheless, without pre-scaling the dissimilarity measure involves a natural size-dependence, that is also providing some advantages in the chemical context. One also may define an asymmetric dissimilarity measure directly, by turning the semi-similarity measures into semi-dissimilarity measures, before symmetrizing by using averages. For example, as illustrated in Figures 2 and 3, one may consider the dissimilarities of water, methanol, and ethanol in terms of molecular isodensity contours (MIDCO's), for example, using the a = 0.1 a.u. (atomic unit) isocontours. Reducing water to fit within ethanol provides a more chemically relevant measure than scaling ethanol to fit within water, yet due to the nearly equivalent sizes of the essential OH groups, a pre-scaling of these two molecules for the same size has very little chemical relevance. One may deduce similar conclusions when considering the other two pairs in this molecular family, water and methanol, or methanol and ethanol. Whereas the sizes of the chemically important common functional groups, in our case, the sizes of the OH groups are rather similar, by themselves not justifying pre-scaling, nevertheless, the sizes of the complete molecules are rather different, and pre-scaling for the complete sizes would cause major size differences in the OH groups, masking their high degree of chemical similarity. Without pre-scaling, one may always adopt the larger of the two scaling factors of the semi-similarity measures as being the chemically more relevant, for example, the scaling factor needed to fit water within ethanol, that would exclude the other scaling factor obtained by the drastic scaling ethanol to fit within water.

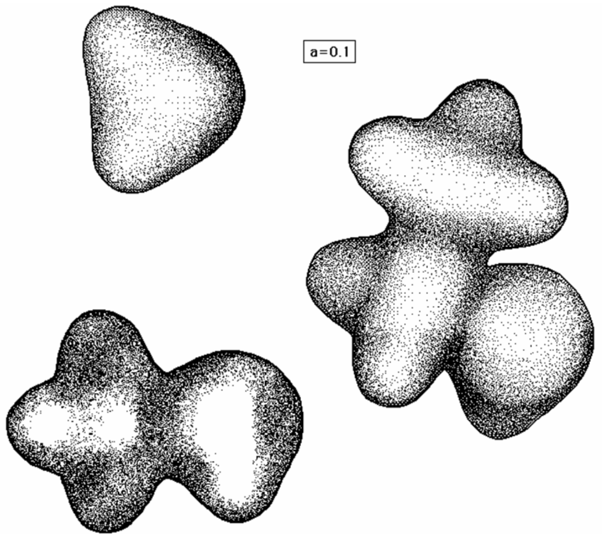

Figure 2. Electron density contours (MIDCO's) for water, methanol, and ethanol, 0.1 a.u. (atomic unit) contours.

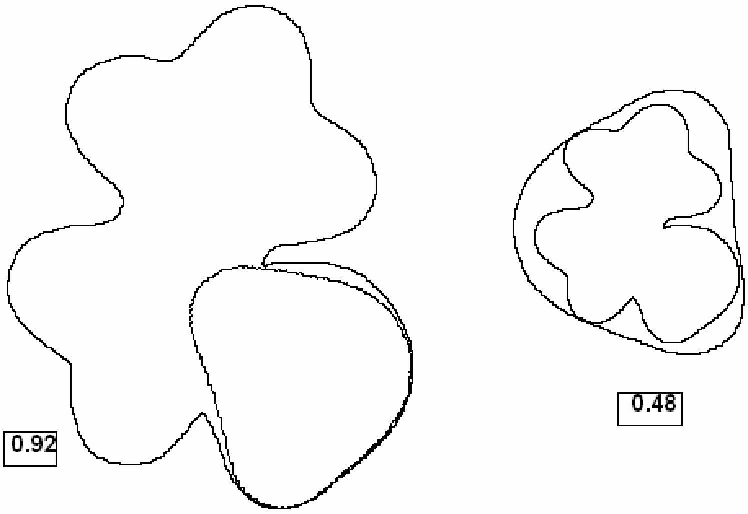

Figure 3. Without pre-scaling, some scaling-nesting relations for molecules of water and ethanol. For the water – ethanol pair, the two semi-similarity scaling factors are 0.92 and 0.48.

In conclusion, neither pre-scaling, nor the scaling of the larger molecule (or, if similarity is evaluated for local electron densities, the larger molecular fragment, or larger functional group) provide a chemically easily interpretable measure, but without pre-scaling, the semi-similarity measure giving the *larger scaling factor* provides the chemically most relevant measure of actual, chemical similarity.

CONCLUSION

It is demonstrated that in some chemical problems the use of semi-similarity measures of the scaling-nesting family of similarity measures, where the pre-scaling step for a common size is avoided, provides a chemically useful similarity measure.

REFERENCES

1. R. Carbó, L. Leyda, M. Arnau, *Int. J. Quantum Chem.* **1980**, *17*, 1185.
2. E. E. Hodgkin, W. G. J. Richards, *Chem. Soc., Chem. Commun.* **1986**, 1342.
3. M. A. Johnson, G. M. Maggiora, *Eds. Concepts and Applications of Molecular Similarity;* Wiley & Sons: New York, **1990**.
4. P. G. Mezey, *J. Chem. Inf: Comput. Sci.* **1992**, *32*, 650.
5. P. G. Mezey, *Shape in Chemistry: An Introduction to Molecular Shape and Topology;* VCH Publishers: New York, **1993**.

6. K. Sen, *Ed. Molecular Similarity, Topics in Current Chemistry*; Springer-Verlag: Heidelberg, **1995**; Vol 173.
7. P. M. Dean, *Ed. Molecular Similarity in Drug Design*; Chapman & Hall - Blackie Publishers: Glasgow, **1995**.
8. R. Carbó, *Ed. Molecular Similarity and Reactivity: From Quantum Chemical to Phenomenological Approaches*; Kluwer Academic Publishers: Dordrecht, The Netherlands, **1995**.
9. E. Besalú, R. Carbó, J. Mestres, M. Solà, *Top. Curr. Chem.,* **1995**, *173*, 31.
10. R. Carbó-Dorca, P. G. Mezey, *Eds. Advances in Molecular Similarity*; JAI Press: Greenwich, Connecticut, **1996**; Vol 1.
11. Y. C. Martin, *Quantitative Drug Design: A Critical Introduction*; Marcel Dekker: New York, **1978**.
12. W. G. Richards, *Quantum Pharmacology*; Butterworths: New York, **1983**.
13. R. Franke, *Theoretical Drug Design Methods*; Elsevier: Amsterdam, **1984**.
14. P. M. Dean, *Molecular Foundations of Drug-Receptor Interaction*; Cambridge University Press: Cambridge, **1987**.
15. P. G. Mezey, *Int. J. Quantum Chem.*, **1994**, *51*, 255.
16. P. G. Mezey, *Int. J. Quantum Chem.*, ***1997***, *63*, 105.
17. P. G. Mezey, *Int. J. Quantum Chem.*, ***1997***, *63*, 39.

STUDIA UNIVERSITATIS BABEŞ-BOLYAI, CHEMIA, LIII, 2, 2008

MECHANISTIC ASPECTS AND BIOCATALYTIC IMPLICATIONS OF THE MIO-CONTAINING AMMONIA-LYASE / AMINOMUTASE FAMILY

LÁSZLÓ POPPE[a], SAROLTA PILBÁK[a],
CSABA PAIZS[b], JÁNOS RÉTEY[c]

ABSTRACT. Histidine, phenylalanine and tyrosine ammonia-lyases (HAL, PAL and TAL) all catalyze ammonia elimination with the aid of a post-translationally formed electrophilic prosthetic group (MIO). MIO occurs also in L-phenylalanine and L-tyrosine aminomutases. Based on the role of PAL as a biocatalyst, the production of β-phenylalanine analogs can be extended with combined use of ammonia-lyases and amino-mutases. For ammonia-lyases two significantly different mechanisms were suggested. One implies an *N*-MIO, whereas the second involves a Friedel-Crafts (FC) type intermediate. A common feature of both mechanisms is the formation of a covalent intermediate which allows systematic confomational analysis of the ligand within the rigid active site. Furthermore QM/MM calculations allowed detailed modeling of the alternative covalent intermediates which demonstrated that the *N*-MIO intermediate has ~140 kcal/mol lower energy than the best FC state.

Keywords: *ammonia-lyase, biocatalysis, covalent intermediate, conformational analysis, QM/MM calculations*

INTRODUCTION

Histidine, phenylalanine and tyrosine ammonia-lyases (HAL, EC 4.3.1.3; PAL, EC 4.3.1.5; TAL, EC 4.3.1.5) catalyze ammonia elimination from L-histidine, L-phenylalanine and L-tyrosine to (*E*)-urocanic acid, (*E*)-cinnamic acid and (*E*)-p-coumaric acid, respectively (Scheme 1).

Under extreme *in vitro* conditions (> 4 M NH_4OH, pH 10) ammonia-lyases catalyze the reverse reaction (amination). The possibility of enantioselective addition to α,β-unsaturated acids made this approach attractive for preparation of L-amino acids by biotransformations [1,2,3,4].

---

[a] *Department of Organic Chemistry and Technology, Budapest University of Technology and Economics, H-1111 Budapest, Gellért tér 4, Hungary, poppe@mail.bme.hu*
[b] *Department of Biochemistry and Biochemical Engineering, Babeş-Bolyai University, Ro-400028 Cluj-Napoca, Arany János 11, Romania*
[c] *Institute of Organic Chemistry, University of Karlsruhe, D-76128, Fritz-Haber Weg 6, Germany*

In spite of the unexplored biocatalytic potential and substrate and substrate tolerance of L-phenylalanine and L-tyrosine aminomutases (PAM and TAM), these enzymes are potential biocatalysts for preparation of optically active ß-amino acids. Whereas PAM isomerizes (2*S*)-α-phenylalanine to (3*R*)-β-phenylalanine with overall retention of configuration of the *pro*-3*R* hydrogen at C_3[5], TAM converts (2*S*)-α-tyrosine to (3*S*)-β-tyrosine [6,7]. These data indicate that the MIO-containing 2,3-aminomutases may proceed through partially different reaction mechanisms.

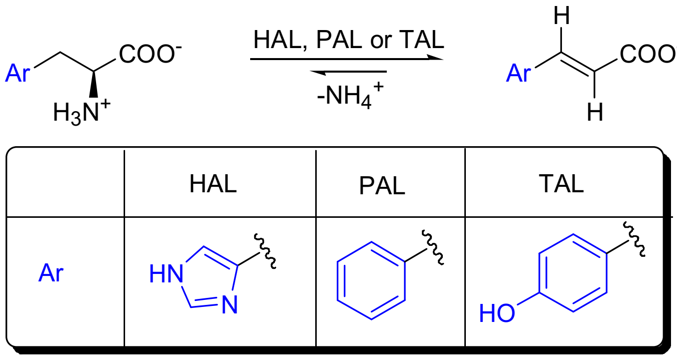

Scheme 1. *The HAL, PAL and TAL reactions.*

Due to its potential as biocatalysts and possible application in treatment of phenylketonuria, PAL was choosen as primary target for detailed investigation of the mode of action at molecular level. For these studies, all the previous mechanistic models and the rapidly growing number X-ray structures of various MIO-enzymes have been used. First, based on HAL X-ray structure we constructed a homology model of parsley PAL for mechanistic calculations [8]. Later, we corrected the Y110-loop of the published X-ray structure of parsley PAL to a mechanistically relevant conformation [9].

RESULTS AND DISCUSSION

The QM/MM calculations were performed within the active site of the well defined experimental structure of *Rhodosporidium toruloides* TAL (*Rs*TAL) [10]. The PAL activity of the analogous His89Phe mutant of *Rs*TAL proved that the TAL and PAL reactions have the same mechanism.

The comparison of the calculated structures and energies of the TAL intermediates with the substrate and product binding states of the enzyme revealed that the *N*-MIO state has a 139 kcal/mol lower energy than the more favorable one of the diastereomeric FC states. Owing to serious distortions the difference for the (*S*)-FC structure is even higher (>10,000 kcal/mol).

In addition, comparison of the calculated structures with the 2-aminoindan-2-phosphonate inhibited *Rs*TAL structure showed that the arrangement of L-tyrosine ligand in the *N*-MIO intermediate is consistent with the overall arrangement found experimentally in the inhibited *Rs*TAL structures [10] i.e. the aromatic moiety points towards His89 and the carboxylate group is to close Arg303.

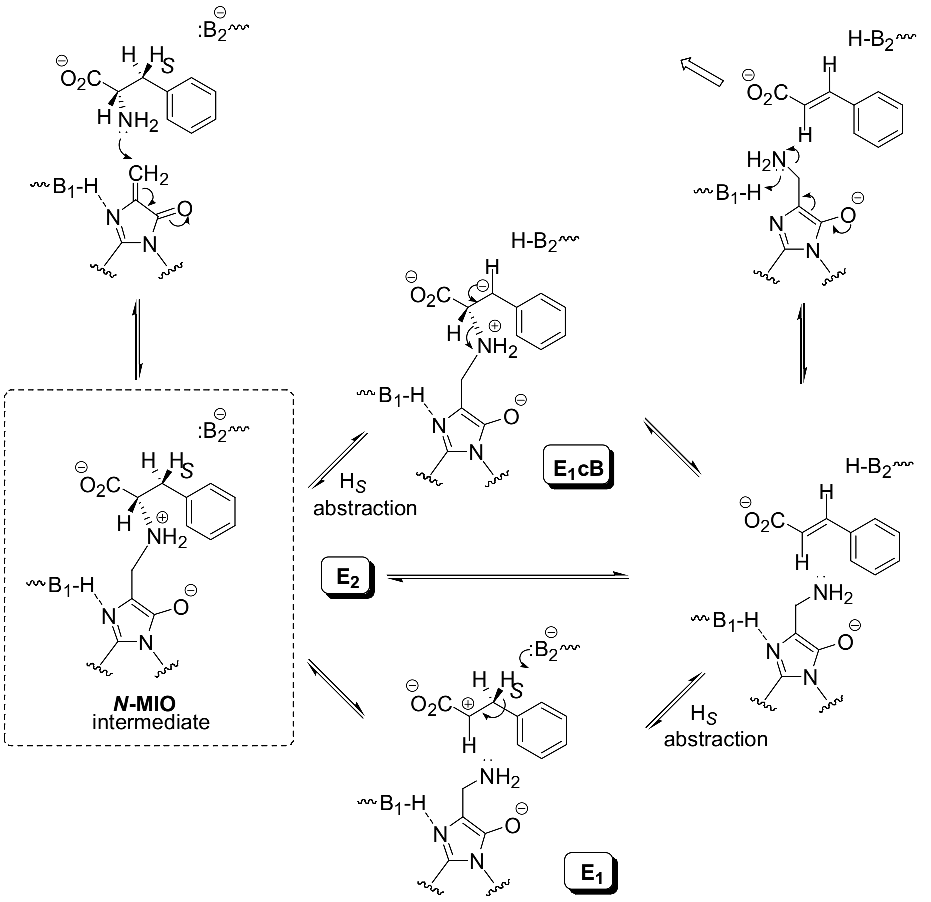

Scheme 2. *Mechanisms of the PAL reaction via an N-MIO intermediate (B$_1$-H: Tyr351/Tyr300 in PAL/ TAL; B$_2$-H: Tyr110/Tyr60 in PAL/TAL).*

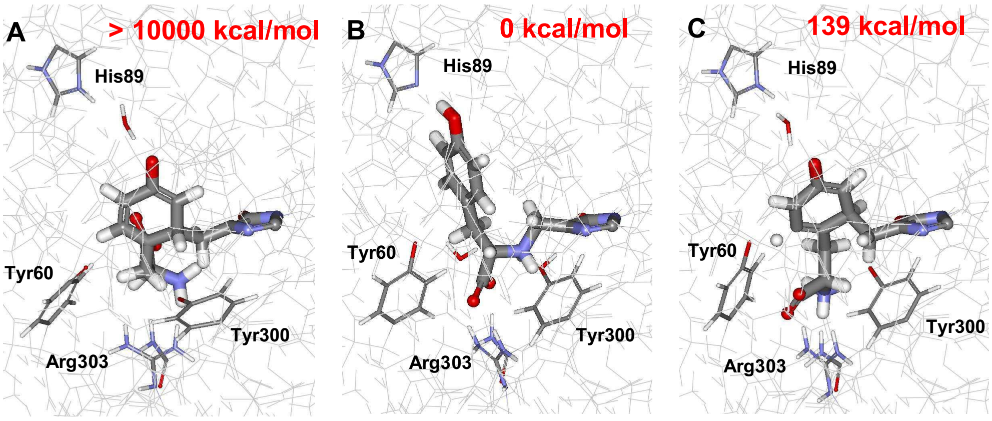

Figure 1. Comparison of the (*S*)-FC (A), *N*-MIO (B) and (*R*)-FC (C) intermediates within the *Rs*TAL active site calculated at PM3/UFF level.

CONCLUSIONS

PAL is a suitable biocatalyst for production of optically pure arylalanines, which can be extended to enantioselective synthesis of β-phenylalanine analogs with combined use of ammonia-lyases and aminomutases.

The QM/MM calculations for the TAL reaction indicated, that a Friedel-Crafts type mechanism can be excluded solely by energetics. The roles of the most important active site residues of *Rs*TAL were explored. His89 and Arg303 anchor the L-tyrosine substrate by hydrogen bonds to its phenolic OH and carboxylate groups, respectively (Figure 1). Tyr300 (B_1) and Tyr60 (B_2) are the two most important enzymic bases (Scheme 2). In the mechanism involving an *N*-MIO intermediate Tyr300 liberates the nucleophilic amino group from its protonated state, whereas Tyr60 has primary importance as the enzymic base responsible for deprotonation at the C_3 *pro-S* side of the substrate.

EXPERIMENTAL SECTION

For the two covalently bound intermediates systematical conformational search (Hyperchem) [11] and QM/MM calculations (Gaussian) [12] were performed within the active site of *Rs*TAL.

REFERENCES

1. JP 63148992, **1988**, ASAHI Glass Co. Ltd.
2. A. Gloge, B. Langer, L. Poppe, J. Rétey, *Arch. Biochem. Biophys.*, **1998**, *359*, 1.
3. A. Gloge, J. Zoń, Á. Kővári, L. Poppe, J. Rétey, *Chem. Eur. J.,* **2000**, *6*, 3386.
4. C. Paizs, A. Katona, J. Rétey, *Chem. Eur. J.*, **2006**, *12*, 2739-2744.
5. W. Mutatu, K. L. Klettke, C. Foster, K. D. Walker, *Biochemistry,* **2007,** *46,* 9785.
6. S. D. Christenson., W. Liu, M. D.Toney, B. Shen,. *J. Am. Chem. Soc.,* **2003**, *125*, 6062.
7. C. V. Christianson, T. J. Montavon, S. G. Van Lanen, B. Shen, S. D. Bruner, *Biochemistry,* **2007,** *46,* 7205.
8. D. Röther, L. Poppe, G. Morlock, S. Viergutz, J. Rétey, *Eur. J. Biochem.,* **2002**, *269*, 3065.
9. S. Pilbák, A. Tomin, J. Rétey, L. Poppe, *FEBS J.,* **2006**, *273*, 1004.
10. G. V. Louie, M. E. Bowman, M. C. Moffitt, T. J. Baiga, B. S. Moore, J. P. Noel, *Chem. Biol.,* **2006**, *13*, 1327.
11. Hyperchem 7.5, Hypercube, Inc., **2003**.
12. Gaussian 03, Revision B.05, M. J. Frisch, *et. al*, Gaussian, Inc., Wallingford CT, **2003**.

STUDIA UNIVERSITATIS BABEŞ-BOLYAI, CHEMIA, LIII, 2, 2008

PROGRESS IN MODELLING ELECTROSTATICS AND POLARIZATION THROUGH EFFECTIVE MULTIPOLES AND INDUCED CHARGES

C. J. R. ILLIGWORTH[a], P. J. WINN[a], G. G. FERENCZY[b], C. A. REYNOLDS*

ABSTRACT. Here we present a method for modeling polarization in hybrid QM/MM calculations. The method, which expresses the induced dipoles as a set of 'induced' charges, is based on the induced dipole approach and methodology for calculating potential-derived point charges from distributed multipole series. Here we assess the importance of explicit polarization in the classical part of a QM/MM system with regard to improving the classical description and the consequent effects on the quantum description. The main advantages of the induced charge approach are that the method is readily interfaced with quantum mechanical methods and that induced charges are more readily interpreted than induced dipoles. The ease of interpretation is illustrated by analysis of the charges involved in dimeric and trimeric hydrogen bonded systems. The method has been validated using two energy decomposition approaches, which show that MM polarization makes a significant and reliable contribution to the QM – MM interaction energy in a hybrid system. The method has been modified to assess the likely effect of QM and MM polarization on docking. Since the lack of polarization is only one of a number of deficiencies in current docking approaches, we have also used connectivity to assess alternative docking poses.

BACKGROUND

Molecular modelling has evolved into a highly versatile research tool in chemistry, biology and materials science. At its heart lies the atomic charge, which contributes to the energetics of the system through Coulomb's law, and while the concept of the atomic charge is relatively simple, implementation is a little more difficult because the atomic charge is not clearly defined in quantum mechanics. Consequently, the early approaches to atomic charges through population analysis of the quantum mechanical wavefunction [1] were not only arbitrary but also failed to yield accurate quantitative results when compared against the more rigorous methods devised (including our own [2]). The electrostatic potential is, however, precisely defined [3], and so the determination of potential derived charges by Kollman [4] for use in force

---

[a] *Department of Biological Sciences, University of Essex, Wivenhoe Park, Colchester, CO1 1NW*
[b] *Department of Inorganic Chemistry and Department of Chemical Information Technology, Budapest University of Technology and Economics, Szent Gellért tér 4, H-1111 Budapest, Hungary*

fields [5], following earlier work by Momany [6], was a significant milestone, enabling applications, such as analysis of the electrostatic potential along the grooves of DNA [7], to proceed from a more rigorous foundation [7]. In parallel with these developments, Stone has presented a far more rigorous approach to electrostatics and polarization [8]. While many of these developments provide a benchmark against which other methods can be tested, they have not found widespread use in biological applications. Nevertheless, Stone's distributed multipole analysis (DMA) [9] is extremely useful. Here we provide a perspective on developments at Essex relevant to modelling biological systems that have been heavily influenced by Stones' DMA. The references cited herein provide a more balanced reference to the many other authors who have inspired developments in this field.

POTENTIAL DERIVED CHARGES

During the 1980s however, ab initio calculations on large molecules were difficult. For this reason, the first program to determine semi-empirical potential derived charges was developed [10], later released through Oxford Molecular. Prior to this, the only option for using semi empirical charges was to use Coulson charges [11], which were essentially similar to Mulliken charges [1]. The essential step in the determination of potential derived charges is usually the constrained minimization of the difference between the quantum mechanical and classical molecular electrostatic potential over a numerical grid at and or beyond the surface of the molecule. This method of determining atomic charges formed the basis of much of our work on calculating molecular properties by free energy difference simulations [12-19].

The use of the numerical grid can lead to asymmetries in the atomic charges of symmetrically equivalent atoms and to poorly defined charges on buried atoms that are well removed from the surface of the molecule [20]. By expanding the wavefunction as a distributed multipole analysis (DMA) and exploiting the properties of spherical harmonics, Ferenczy was able to replace the numerical summation over the grid by an analytical integral over a spherical shell surrounding the centre of each multipole series [21]. This method forms the basis of much of our work on modelling polarization through induced charges [20, 22-27] and does not suffer from the known problems of standard potential derived charges [20].

The availability of readily determined semi-empirical potential derived charges enabled a number of molecular mechanics drug-enzyme studies to be completed, most notably the binding of bioreductive DNA minor groove binding ligands [28].

Free energy simulations, however, provided a greater challenge. For example, while determination of the relative partition coefficients of methanol and ethanol could be carried out relatively easily [15], the corresponding ethanol-propanol system could only be studied [29] through the use of potential derived charges that were valid across a range of conformations [30,31] (this was achieved by weighting the elements of the potential by the Boltzmann population of the conformations from which they were derived). These multiple conformation charges later formed the basis of widely used AMBER force fields [32]. The early potential derived charges were determined using Hartree-Fock wave functions. The fact that the Hartree-Fock wavefunction renders a molecule slightly too polar is fortuitous as it has the effect of including polarization implicitly. The resultant error in the hydration energy arising from a molecule being too polar can be estimated by comparison against charge distributions derived from correlated wavefunctions [22], and this is indeed of the same order (~10-15%) as the polarization energy [22], implying that biological force fields should be based on correlated wavefunctions if they include polarization explicitly [22].

One advantage of the multipole-derived charges, that has not been extensively exploited to date, is the possibility of determining effective multipoles, i.e. charges plus dipoles or charges, dipoles and quadrupoles as these are highly efficient when compared to the underlying DMA in that charges plus dipoles from effective multipoles are roughly equivalent (in determining interaction energies) to octopoles or hexadecapoles from the DMA [23].

POLARIZATION

The classical way to include polarization in a molecular mechanics force field is to use induced dipoles.

$$\mu = \alpha \boldsymbol{E}$$

where μ is the induced dipole at a given atom, α is the isotropic polarizability of the atom and $\boldsymbol{E}$ is the electric field at the atom. The electric field, $\boldsymbol{E}$, depends on all the other atomic charges and induced dipoles and so the equations are usually solved iteratively. The method is complicated and computationally expensive as the induced dipole is a vector and hence the energy evaluations are inherently more complex. The method is also intellectually inconsistent as the smaller polarization component is handled at the higher dipole (rank 1) level whereas the more important electrostatic component is handled at the lower atomic charge (rank 0) level.

However, the software used in the determination of the multipole-derived charges can be exploited to model polarization since the ability to convert a multipole series into a distributed charge distribution can be used to convert an induced dipole (which is a very simple multipole series) into a set of induced charges on the given atom hosting the induced dipole and those atoms connected to it. There are four distinct advantages of this approach. Firstly, the induced charges are easier to interpret than induced dipoles and so have more value in aiding chemical intuition [20, 24, 26]. Secondly, induced charges are easier to implement in a variety of other programs and so they can be use to implement for example MM polarization in hybrid QM/MM methods [20, 26]. Thirdly, induced charges are not as computationally expensive as induced dipoles [27] and fourthly, the induced charges are fully consistent with the derivation of most force fields that use quantum mechanical potential derived charges since the induced charges are essentially potential derived charges. For this reason, benchmarking against quantum mechanical calculations has played a key role in developing this approach [20, 24].

The initial implementation of the method focused on a comparison of the induced charges in a number of small molecule complexes (dimers and trimers) with those determined quantum mechanically; considerable quantitative agreement was obtained [24], though this agreement cannot be taken too far as the induced dipole at a point is replaced by a set of charges at the point and its bonded neighbours [20]. Nevertheless, this agreement included reproduction of the slightly enhanced or slightly suppressed induced charges that may occur in cooperative and anti-cooperative hydrogen bonding systems, as illustrated in Figure 1 for water dimers and trimers; these effects have also been reproduced in hybrid QM/MM systems [20].

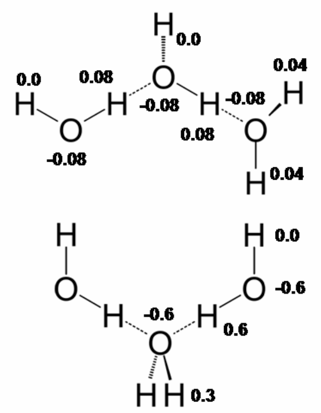

Figure 1. A comparison of the induced charges in a cooperative water trimer (top) and an anti-cooperative water trimer (bottom). The magnitude of the (idealized) induced charges is higher in the cooperative system.

Our first QM/MM implementation of induced charges was used in an investigation into the non-bonded iodine-oxygen interaction in dimethyl-2-iodobenzoylphosphonate, since the oxygen and iodine atoms both approach very close to each other, despite being on the same side of the periodic table and hence both formally electronegative; it was concluded that the high polarizability of the iodine greatly softened the iodine-oxygen electrostatic repulsion [26]. The potential of the method can be illustrated by two further applications of the QM/MM(IC) method, i.e. the inclusion of induced charges in the molecular mechanics part of a hybrid QM/MM calculation. Within QM/MM(IC) methods, the determination of the field at the MM atoms is more efficient if the wavefunction is expanded as a DMA since the field can then be calculated using Orient [33].

The first involved a study of the contribution of enzyme polarization to transition state stabilization within the enzyme chorismate mutase. Using the previously published structures, we were able to show that the extent of polarization within the enzyme transition state was very similar to that in the reactant geometry [34], and hence that in these particular geometries polarization did not contribute to transition state polarization.

The second study assessed the potential of including MM polarization in docking. Docking programs are design to be computationally efficient rather than accurate and so generally use empirical charges such as those proposed by Gasteiger [35]. Cho et al. have shown that there are distinct advantages for increasing accuracy in using potential derived charges, particularly when the ligand is polarized by the enzyme [36]. At a simple level, this approach requires knowledge of the final answer so that the ligand can be correctly polarized by the enzyme, but the authors have developed a survival of the fittest approach that does not require knowledge of the answer a priori. Against, this background, we have extended this approach to include polarization of the enzyme by the ligand. The ligand was treated quantum mechanically to avoid parameterization issues [37], but in principle, the way to extend this to a fully classical system has already been determined [24]. The method was tested on 10 systems that had previously presented difficulties in Autodock docking experiments. In some cases clear improvements were observed. For example, with the protein - ligand complex from PDB structure 9AAT, the RMS for docking 4'-deoxy-4'-aminopyridoxal-5'-phosphate to mitochondrial aspartate aminotransferase in autodock using the default Gasteiger electrostatics was 7 Å, but with polarization fully included the RMS dropped to 0.9 Å. Not all of the systems showed such clear improvements but clear criteria for assessing when an improvement in the methodology gave rise to an improvement in the results could be determined by analysis of the clustering results.

The previous two applications involved single point determinations of the induced charges since the multipole derived charge methodology [21] cannot readily be extended to include derivatives of the charges. Consequently, a variation on the method has been developed that is suitable for implementation in molecular dynamics simulations [27]. Using only one adjustable parameter and by modifying the TIP3P water model to include induced charges, we were able to reproduce the oxygen-oxygen radial distribution function for water remarkably well. Moreover, the method is actually based on determination of the potential rather than the field. This article highlighted a problem with induced charges. When the field is perpendicular to the plane, then without the addition of off-atom sites (which can be readily added) the model is not sufficiently flexible to fully reproduce the polarization. However, in a further application we have shown that the extent of polarization energy determined using the induced charge model is generally in line with that determined using a quantum mechanical energy decomposition analysis with medium sized basis sets. In other words, the small amount of polarization energy lost by using induced charges (without off-atom sites) rather than induced dipoles fortuitously corresponds to the amount of polarization energy lost when using a medium sized basis set rather than a large basis set with multiple diffuse functions). The polarization energy determined using the induced dipole model is generally only comparable to that determined using a quantum mechanical energy decomposition analysis when very large basis sets are used that include diffuse functions. This suggests that induced charges are more appropriate for inclusion in QM/MM calculations on biological systems where very large basis sets are generally too expensive [38].

Throughout the development of these methods the possibility of comparison against more rigorous methods such as quantum mechanical calculations, QM/MM calculations or DMA-derived energies has played a key role.

REFERENCES

1. R.S. Mulliken, *J. Chem. Phys.* **1955**, *23*, 1833.
2. C.A. Reynolds, G.G. Ferenczy, W.G. Richards, *Theochem-J. Mol. Struct.* **1992**, *88*, 249.
3. R. Bonaccorsi, E. Scrocco, J. Tomasi, *J. Chem. Phys.* **1970**, *52*, 5270.
4. U.C. Singh, P.A. Kollman, *J. Comput. Chem* **1984**, *5*, 129.
5. S.J. Weiner, P.A. Kollman, D.A. Case, U.C. Singh, C. Ghio, G. Alagona, S. Profeta, P.A. Weiner, *J. Amer. Chem. Soc.* **1984**, *106*, 765.
6. F.A. Momany, *J. Phys. Chem.* **1978**, *82*, 592.
7. J.M. Burridge, P. Quarendon, C.A. Reynolds, P.J. Goodford, *J. Mol. Graphics.* **1987**, *5*, 165.
8. A.J. Stone, The theory of intermolecular forces. Oxford University Press, 1996.
9. A.J. Stone, *Chem. Phys. Lett.* **1981**, *83*, 233.
10. G.G. Ferenczy, C.A. Reynolds, W.G. Richards, *J. Comput. Chem.* **1990**, *11*, 159.

11. B.H. Chirguin, C.A. Coulson, *Proc. R. Soc. London. Ser. A.* **1950**, *201*, 196.
12. S.G. Lister, C.A. Reynolds, W.G. Richards, *Int. J. Quantum Chem.* **1992**, *41*, 293.
13. C.A. Reynolds, P.M. King, W.G. Richards, *Chem. Comm.* **1988**, 1434.
14. C.A. Reynolds, P.M. King, W.G. Richards, *Nature* **1988**, *334*, 80.
15. J.W. Essex, C.A. Reynolds, W.G. Richards, *Chem. Comm.* **1989**, 1152.
16. M.C. Menziani, C.A. Reynolds, W.G. Richards, *Chem. Comm.* **1989**, 853.
17. R.G. Compton, P.M. King, C.A. Reynolds, W.G. Richards, A.M. Waller, *J. Electroanal. Chem.* **1989**, *258*, 79.
18. P.M. King, C.A. Reynolds, W.G. Richards, *J. Mol. Struct. (THEOCHEM)* **1990**, *67*, 205.
19. P.M. King, C.A. Renolds, J.W. Essex, G.A. Worth, W.G. Richards, *Mol. Sim.* **1990**, *5*, 265.
20. C.J. Illingworth, S.R. Gooding, P.J. Winn, G.A. Jones, G.G. Ferenczy, C.A. Reynolds, *J. Phys. Chem. A* **2006**, *110*, 6487.
21. G.G. Ferenczy, *J. Comput. Chem.* **1991**, *12*, 913.
22. P.J. Winn, G.G. Ferenczy, C.A. Reynolds, *J. Phys. Chem. A* **1997**, *101*, 5437.
23. G.G. Ferenczy, P.J. Winn, C.A. Reynolds, *J. Phys. Chem. A* **1997**, *101*, 5446.
24. P.J. Winn, G.G. Ferenczy, C.A. Reynolds, *J. Comput. Chem.* **1999**, *20*, 704.
25. J.H. Wu, P.J. Winn, G.G. Ferenczy, C.A. Reynolds, *Int. J. Quant. Chem.* **1999**, *73*, 229.
26. S.R. Gooding, P.J. Winn, R.I. Maurer, G.G. Ferenczy, J.R. Miller, J.E. Harris, D.V. Griffiths, C.A. Reynolds, *J. Comput. Chem.* **2000**, *21*, 478.
27. G.G. Ferenczy, C.A. Reynolds, *J. Phys. Chem. A* **2001**, *105*, 11470.
28. I.S. Haworth, C. Burt, F. Gago, C.A. Reynolds, W.G.A. Richards, *Anti-Cancer Drug Des.* **1991**, *6*, 59.
29. J.W. Essex, C.A. Reynolds, W.G. Richards, *J. Amer. Chem. Soc.* **1992**, *114*, 3634.
30. C.A. Reynolds, J.W. Essex, W.G. Richards, *J. Amer. Chem. Soc.* **1992**, *114*, 9075.
31. C.A. Reynolds, J.W. Essex, W.G. Richards, *Chem. Phys. Lett.* **1992**, *199*, 257.
32. W.D. Cornell, P. Cieplak, C.I. Bayly, I.R. Gould, K.M. Merz, D.M. Ferguson, D.C. Spellmeyer, T. Fox, J.W. Caldwell, P.A. Kollman, *J. Amer. Chem. Soc.* **1995**, *117*, 5179.
33. A.J. Stone, A. Dullweber, O. Engkvist, E. Fraschini, M.P. Hodges, A.W. Meredith, D.R. Nutt, P.L.A. Popelier, D.J. Wales, (2002) Orient: a program for studying interactions between molecules, version 4.5', University of Cambridge, Enquiries to AJ Stone, ajs1@cam.ac.uk. 2006.
34. C.J.R. Illingworth, K.E. Parkes, C.R. Snell, S. Marti, V. Moliner, C.A. Reynolds, *J. Phys. Chem. A., in press,* **2008**.
35. J. Gasteiger, M. Marsili, *Tet. Lett.* **1978**, 3181.
36. A.E. Cho, V. Guallar, B.J. Berne, R. Friesner, *J Comput. Chem.* **2005**, *26*, 915.
37. C.J.R. Illingworth, G.M. Morris, K.E.B. Parkes, C.R. Snell, C.A. Reynolds, *J. Phys. Chem. A., in press*.
38. C.J.R. Illingworth, K.E.B. Parkes, C.R. Snell, G.G. Ferenczy, C.A. Reynolds, *J. Phys. Chem. A., in press*.

STUDIA UNIVERSITATIS BABEŞ-BOLYAI, CHEMIA, LIII, 2, 2008

UNSATURATION IN BINUCLEAR FIRST ROW CYCLOPENTADIENYLMETAL CARBONYLS AS STUDIED BY DENSITY FUNCTIONAL THEORY

R. BRUCE KING[a], HENRY F. SCHAEFER[a], YAOMING XIE[a],
QIAN-SHU LI[b], XIUHUI ZHANG[b], HONGYAN WANG[c]

ABSTRACT. The geometries of binuclear cyclopentadienylmetal carbonyls $Cp_2M_2(CO)_n$ as well as related metal nitrosyl and cyclobutadienemetal derivatives have been optimized by using B3LYP and BP86 methods from density functional theory. New examples of metal-metal multiple bonding and four-electron donor carbonyl groups have been found in unsaturated molecules of this type.

Keywords: *metal carbonyls, metal nitrosyls, cyclopentadienylmetal derivatives, cyclobutadienemetal derivatives, metal-metal bonding, DFT calculations.*

INTRODUCTION

The first example of an unsaturated metal carbonyl derivative was the molybdenum complex $(\eta^5\text{-}Me_5C_5)_2Mo_2(CO)_4$ first synthesized by King and Bisnette [1] in 1967 and structurally characterized by Huang and Dahl [2] a number of years later. The relatively short Mo≡Mo distance of 2.488 Å found in this complex was interpreted to be the metal-metal triple bond required to give both metal atoms the favored 18-electron rare gas electronic configuration. Subsequently other unsaturated binuclear cyclopentadienylmetal carbonyl derivatives with formal metal-metal triple bonds such as $(\eta^5\text{-}C_5R_5)_2V_2(CO)_5$,[3,4] $(\eta^5\text{-}C_5R_5)_2Cr_2(CO)_4$, [5,6,7] and $(\eta^5\text{-}C_5R_5)_2M'_2(CO)_3$ (M´= Mn, [8] Re [9]) were synthesized. In addition, $Cp_2Co_2(CO)_2$ [10] and $Cp_2Fe_2(CO)_3$ [11] with formal metal-metal double bonds have been synthesized and characterized structurally. Table 1 summarizes the possible unsaturated binuclear cyclopentadienylmetal carbonyls of the first row transition metals listed according to the formal metal-metal bond order assuming 18-electron configurations for the metal atoms and only two-electron donor carbonyl groups. Compounds in Table 1 that are sufficiently stable for isolation and structural characterization by X-ray diffraction are listed in **bold** type.

---

[a] *Department of Chemistry and Center for Computational Chemistry, University of Georgia, Athens, Georgia, USA, rbking@chem.uga.edu*
[b] *Institute of Chemical Physics, Beijing Institute of Technology, Beijing 100081, P. R. China*
[c] *College of Sciences, Southwest Jiaotong University, Chengdu 610031, P. R. China*

Table 1.

Possible unsaturated cyclopentadienylmetal carbonyls of the first row transition metals

M–M	M=M	M≡M	$M_{=},^{=}M$
$Cp_2Ti_2(CO)_8$	$Cp_2Ti_2(CO)_7$	$Cp_2Ti_2(CO)_6$	$Cp_2Ti_2(CO)_5$
$Cp_2V_2(CO)_7$	$Cp_2V_2(CO)_6$	**$Cp_2V_2(CO)_5$**	$Cp_2V_2(CO)_4$
$Cp_2Cr_2(CO)_6$	$Cp_2Cr_2(CO)_5$	**$Cp_2Cr_2(CO)_4$**	$Cp_2Cr_2(CO)_3$
$Cp_2Mn_2(CO)_5$	$Cp_2Mn_2(CO)_4$	**$Cp_2Mn_2(CO)_3$**	$Cp_2Mn_2(CO)_2$
$Cp_2Fe_2(CO)_4$	**$Cp_2Fe_2(CO)_3$**	$Cp_2Fe_2(CO)_2$	$Cp_2Fe_2(CO)$
$Cp_2Co_2(CO)_3$	**$Cp_2Co_2(CO)_2$**	$Cp_2Co_2(CO)$	
$Cp_2Ni_2(CO)_2$	$Cp_2Ni_2(CO)$		
$Cp_2Cu_2(CO)$			

Stable metal carbonyl derivatives usually have 18-electron configurations corresponding to filling each the nine orbitals of the sp^3d^5 valence orbital manifold with electron pairs. Unsaturated binuclear metal carbonyls and cyclopentadienylmetal carbonyls may be regarded as analogues of ethylene and acetylene. Whereas the unsaturation in ethylene and acetylene always leads to carbon-carbon double and triple bonds in stable compounds, unsaturation in metal carbonyl derivatives can, at least in principle, be manifested in several different ways including the following: (1) Formation of metal-metal multiple bonds retaining the favored 18-electron metal configuration; (2) Four-electron bridging carbonyl groups involving not only donation of an electron pair through a carbon-metal dative σ-bond but also donation of a second electron pair from a filled π orbital of the $C{\equiv}O$ triple bond in a carbonyl ligand; (3) Metal electronic configurations less than 18 electrons of which a 16-electron configuration for d^8 metal atoms is the most common. Unsaturated binuclear metal carbonyls $M_2(CO)_n$ containing only carbonyl ligands are not stable and have only been observed in low-temperature matrices. However, a number of unsaturated cyclopentadienylmetal carbonyls are stable as indicated above.

This paper summarizes some of our recent work on cyclopentadienylmetal carbonyl derivatives of first row transition metals V, [12,13] Cr, [14] Fe,[15] Co, [16] Ni [17] as well as related cyclobutadienylmetal nitrosyl[17] and cyclobutadiene cobalt carbonyl [18] derivatives. It is based on a lecture by RBK given at the MOLMOD 2007 conference held at Arcalia near Bistrița in July, 2007. At the time of the conference our work on binuclear cyclopentadienylmanganese carbonyls [19] was not complete so they were not discussed in this lecture and thus are not included in this paper.

THEORETICAL METHODS

Two DFT functionals were used in this work. The first functional is the B3LYP method, which is the hybrid HF/DFT method using the combination of the three-parameter Becke functional (B3) with the Lee-Yang-Parr (LYP) generalized gradient correlation functional [20,21]. The other DFT method used was BP86, which combines Becke's 1988 exchange functional (B) with Perdew's 1986 gradient corrected correlation functional method (P86) [22,23]. All calculations were performed using the double-ζ plus polarization (DZP) basis sets. The DZP basis sets used for carbon and oxygen add one set of pure spherical harmonic d functions with orbital exponents $\alpha_d(C) = 0.75$ and $\alpha_d(O) = 0.85$ to the standard Huzinaga-Dunning contracted DZ sets [24,25] and are designated as 9s5p1d/4s2p1d.. For hydrogen, a set of p polarization functions $\alpha_p(H) = 0.75$ is added to the Huzinaga-Dunning DZ set. The loosely contracted DZP basis set for the transition metals is the Wachters primitive set [26] augmented by two sets of p functions and one set of d functions, contracted following Hood, Pitzer, and Schaefer,[27] designated (14s11p6d/ 10s8p3d).

RESULTS AND DISCUSSION

The results with the binuclear cyclopentadienylmetal carbonyls can be summarized as follows:

(1) $Cp_2Ni_2(CO)_n$. The experimentally known [28] doubly bridged structure was found to be the lowest energy structure for $Cp_2Ni_2(CO)_2$ with alternative triplet structures having considerably higher energies. Singly bridged structures were found to be of lowest energy for $Cp_2Ni_2(CO)$.

(2) $Cp_2Co_2(CO)_n$. For $Cp_2Co_2(CO)_3$ singly bridged and triply bridged structures with formal Co–Co single bonds have similar energies; the singly bridged structure is the one known experimentally [29]. The strongly preferred structure for $Cp_2Co_2(CO)_2$ is the doubly bridged structure with a formal Co=Co double bond; this structure has also been realized experimentally.[10] The preferred structure for $Cp_2Co(CO)$ is a singly bridged structure with a formal Co≡Co triple bond. This species has not been isolated but is a probable reaction intermediate in the pyrolysis [30] of $Cp_3Co_3(\mu\text{-}CO)_3$ to give the tetranuclear derivative $Cp_4Co_4(\mu_3\text{-}CO)_2$.

(4) $Cp_2Fe_2(CO)_n$. The *trans-* and *cis*-$Cp_2Fe_2(CO)_2(\mu\text{-}CO)_2$ isomers of $Cp_2Fe_2(CO)_4$ known experimentally are predicted to be genuine minima with very similar energies consistent with the experimental observation of an equilibrium between these isomers in solution [31-34]. An intermediate in the interconversion

of the *trans*- and *cis*-$Cp_2Fe_2(CO)_2(\mu\text{-}CO)_2$ doubly bridged isomers of $Cp_2Fe_2(CO)_4$ can be the *trans* unbridged isomer of $Cp_2Fe_2(CO)_4$ calculated to be 2.3 kcal/mole (B3LYP) or 9.1 kcal/mole (BP86) above the global minimum *trans*-$Cp_2Fe_2(CO)_2(\mu\text{-}CO)_2$. For the unsaturated $Cp_2Fe_2(CO)_3$ the known[11] triplet isomer $Cp_2Fe_2(\mu\text{-}CO)_3$ with an Fe=Fe double bond similar to the O=O double bond in O_2 is found to be the global minimum. The lowest energy structure for the even more unsaturated $Cp_2Fe_2(CO)_2$ is a doubly bridged structure $Cp_2Fe_2(\mu\text{-}CO)_2$ with a short iron-iron distance suggesting the Fe≡Fe triple bond required to give both iron atoms the favored 18-electron configuration. This species has not been synthesized but is a probable reaction intermediate in the pyrolysis of $Cp_2Fe_2(CO)_2(\mu\text{-}CO)_2$ to give $Cp_4Fe_4(\mu_3\text{-}CO)_4$ [31]. The lowest energy structure for $Cp_2Fe_2(CO)$ is a triplet unsymmetrically bridged structure $Cp_2Fe_2(\mu\text{-}CO)$ with a short iron-iron distance (~2.1 Å) suggestive of the Fe$^{=}$,=Fe quadruple bond required to give both iron atoms the favored 18-electron rare gas configuration.

(5) $Cp_2Cr_2(CO)_n$. The experimentally realized structures of the stable singlet $Cp_2Cr_2(CO)_6$ with a formal Cr–Cr single bond and singlet $Cp_2Cr_2(CO)_4$ with a formal Cr≡Cr triple bond correspond to the global minima found by DFT methods [14]. The global minimum for $Cp_2Cr_2(CO)_5$, expected to have a formal Cr=Cr double bond, is a triplet, which is thermodynamically unstable with respect to disproportionation into the stable $Cp_2Cr_2(CO)_6$ and $Cp_2Cr_2(CO)_4$ with formal Cr–Cr single and Cr≡Cr triple bonds, respectively. This instability of $Cp_2Cr_2(CO)_5$ has been verified experimentally [14]. Triplet and singlet structures are found for the tricarbonyl $Cp_2Cr_2(CO)_3$ with the triplet isomer having an apparent Cr≡Cr triple bond (2.295 Å by BP86) predicted to have lower energy than the singlet isomer having an apparent Cr$^{=}$,=Cr quadruple bond (2.191 Å by BP86). Quintet, septet, and singlet structures as well as a highly spin contaminated triplet structure were found for the dicarbonyl $Cp_2Cr_2(CO)_2$. In all of the $Cp_2Cr_2(CO)_n$ ($n = 3, 2$) structures the carbonyls are asymmetric semibridging groups, typically with differences of 0.3 to 0.5 Å between the shortest and longest M–C distances.

(6) $Cp_2V_2(CO)_n$. An optimized structure for $Cp_2V_2(CO)_7$ is found with one symmetrical bridging carbonyl group and a V–V distance of 3.306 Å (BP86) suggesting a single bond [12]. This structure is predicted to be unstable with respect to dissociation into $CpV(CO)_4$ + $CpV(CO)_3$. Energetically competitive structures for $Cp_2V_2(CO)_6$ include a doubly symmetrically bridged singlet structure with only two-electron donor carbonyl groups, a triplet doubly semibridged structure, and a singlet structure with one four-electron donor bridging carbonyl group [12]. The global minimum for $Cp_2V_2(CO)_5$ with a V≡V distance of 2.452 Å (BP86) [13] is essentially the same as the structure

of the known $Cp_2V_2(CO)_5$ determined by X-ray diffraction [14]. The global minimum for $Cp_2V_2(CO)_4$ is a triplet electronic state with a $V\equiv V$ distance of 2.444 Å (BP86). However, slightly higher energy singlet $Cp_2V_2(CO)_4$ structures are found either with a $V\equiv V$ distance of 2.547 Å (BP86) and one four-electron donor bridging CO group or with a $V^{=},{=}V$ distance of 2.313 Å (BP86) and all two-electron donor bridging CO groups. Four-electron donor bridging carbonyl groups become more prevalent upon further decarbonylation leading ultimately to three singlet $Cp_2V_2(\eta^2\text{-}\mu\text{-}CO)_2$ isomers as well as triplet, quintet, and septet structures of $Cp_2V_2(CO)$ with extremely low $\nu(CO)$ frequencies around 1400 cm^{-1}.

Similar DFT studies were also performed on the binuclear cyclobutadienecobalt carbonyl derivatives[18] $(\eta^4\text{-}C_4H_4)_2Co_2(CO)_n$ (n = 4, 3, 2, 1) for comparison with the isoelectronic $Cp_2Fe_2(CO)_n$ derivatives discussed above. The singlet doubly bridged and unbridged isomers of $(\eta^4\text{-}C_4H_4)_2Co_2(CO)_4$ are nearly degenerate suggesting a highly fluxional system similar to the experimentally known and closely related $(\eta^5\text{-}C_5H_5)_2Fe_2(CO)_4$ and $(\eta^4\text{-diene})_2Co_2(CO)_4$ systems. The global minimum of $(C_4H_4)_2Co_2(CO)_3$ is a doubly bridged singlet isomer $(\eta^4\text{-}C_4H_4)_2Co_2(CO)(\mu\text{-}CO)_2$ in contrast to the isoelectronic $(C_5H_5)_2Fe_2(CO)_3$ where the global minimum is a triply bridged triplet isomer $(\eta^5\text{-}C_5H_5)_2Fe_2(\mu\text{-}CO)_3$ analogous to dioxygen. A related triply bridged triplet isomer of $(C_4H_4)_2Co_2(CO)_3$ is also found, but at 9.6 kcal/mol (B3LYP) or 5.1 kcal/mol (BP86) above the global minimum. The $(C_4H_4)_2Co_2(CO)_2$ system behaves analogously to the corresponding $(C_5H_5)_2Fe_2(CO)_2$ system in that its lowest energy structure is a doubly bridged isomer $(\eta^4\text{-}C_4H_4)_2Co_2(\mu\text{-}CO)_2$ with a short cobalt-cobalt distance suggestive of the $Co\equiv Co$ triple bond required to give both cobalt atoms the favored 18-electron configuration. Both axial and perpendicular metallocene structures are found for $(C_4H_4)_2Co_2(CO)$, including a low energy $(\eta^4\text{-}C_4H_4)_2Co_2(\eta^2\text{-}\mu\text{-}CO)$ structure with a four-electron donor bridging CO group and a cobalt-cobalt distance suggestive of a $Co\equiv Co$ triple bond.

Some DFT studies on binuclear late transition metal cyclopentadienylmetal nitrosyls $Cp_2M_2(NO)_n$ (M = Fe, Co, Ni) were also carried out for comparison with related carbonyl derivatives.[17] However, in such metal nitrosyls the neutral NO ligands can formally be either three-electron or one-electron donors. For terminal NO groups, three-electron donors have linear $M–N\equiv O$ configurations whereas one-electron donors have bent $M–N=O$ configurations. Similarly for bridging NO groups three electron donors have planar M_2NO configurations whereas one-electron donors have pyramidal M_2NO configurations. The global minima for $Cp_2M_2(NO)_2$ (M = Fe, Co) are found to have closely related structures with two symmetrically bridging nitrosyl ligands but variable planarity of the central M(μ-NO)$_2$M units. Similarly the single nitrosyl ligands in the global minima for $Cp_2M_2(NO)$ are found to bridge symmetrically the pair of metal atoms. An unusual dimer Cp_2Ni_2(μ-NO)$_2$ was found with a Ni–Ni bond distance suggestive of a single bond and geometry corresponding to one one-electron donor bridging NO group and one three-electron donor bridging NO group. However, dissociation of Cp_2Ni_2(μ-NO)$_2$ into the well-known stable monomer CpNiNO is highly favored energetically.

CONCLUSIONS

Structures with metal-metal multiple bonds are preferred over structures with four-electron donor bridging carbonyl groups for the $Cp_2M_2(CO)_n$ derivatives studied in this work except for highly unsaturated derivatives of the early transition metal vanadium. Among these structures, those with formal M≡M triple bonds appear to be particularly favorable and are found in a number of stable $Cp_2M_2(CO)_n$ derivatives such as $Cp_2V_2(CO)_5$, $Cp_2Cr_2(CO)_4$, and $Cp_2Mn_2(CO)_3$. Furthermore, $Cp_2Cr_2(CO)_5$, with a formal Cr=Cr double bond is known both experimentally and theoretically to disproportionate into $Cp_2Cr_2(CO)_6$ and $Cp_2Cr_2(CO)_4$ with Cr–Cr single and Cr≡Cr triple bonds, respectively.

ACKNOWLEDGMENTS

We are indebted to the the U. S. National Science Foundation (Grants CHE-0209857, CHE-0451445, and CHE-0716718) for support of the work at the University of Georgia, the 111 Project (B07012) in China for the support of the work at the Beijing Institute of Technology, and the Chinese National Science Foundation (Grant 10774104) for the support of the portion of the work at Southwest Jiaotong University.

REFERENCES

1. R. B. King, M. B. Bisnette, *J. Organometal. Chem.* **1967**, *8*, 129.
2. J. S.Huang, L. F. Dahl, *J. Organometal. Chem.* **1983**, *243*, 57.
3. F. A. Cotton, L. Kruczynski, B. A. Frenz, *J. Organometal. Chem.* **1978**, *160*, 93.
4. J. C. Huffman, L. N. Lewis, K. G. Caulton, *Inorg. Chem.* **1980**, *19*, 2755.
5. M. D. Curtis, W. M. Butler, *J. Organometal. Chem.* **1978**, *155*, 131.
6. R. B. King, A. Efraty, W. M. Douglas, *J. Organometal. Chem.* **1973**, *60*, 125.
7. J. Potenza, P. Giordano, D. Mastropaolo, A. Efraty, *Inorg. Chem.* **1974**, *13*, 254.

8. W. A. Herrmann, R. Serrano, J. Weichmann, *J. Organometal. Chem.* **1983**, *246*, C57.
9. J. K. Hoyano, W. A. G. Graham, *Chem. Comm*. **1982***,* 27.
10. W. I. Bailey Jr., D. M. Collins, F. A. Cotton, J. C. Baldwin, *J. Organometal. Chem.* **1979**, *165*, 373.
11. J. P. Blaha, B. E. Bursten, J. C. Dewan, R. B. Frankel, C. L. Randolph, B. A. Wilson, M. S. Wrighton, *J. Am. Chem. Soc.* **1985**, *107*, 4561.
12. Q. Li, X. Zhang, Y. Xie, R. B. King, H. F. Schaefer, III *Eur. J. Inorg. Chem.*, **2007**, 1599.
13. QLi, X. Zhang, Y. Xie, R. B. King, H. F. Schaefer, *J. Am. Chem. Soc.*, **2007***, 129*, 3433.
14. G. C. Fortman, T. Kégl, Q.-S. Li, X. Zhang, H. F. Schaefer, Y. Xie, R. B. King, J. Telser, C. D. Hoff, *J. Am. Chem. Soc.*, **2007**, *129*, 14388.
15. H. Y. Wang, Y. Xie, R. B. King, H. F. Schaefer, *Inorg. Chem.*, **2006**, *45*, 3384.
16. H. Wang, Y. Xie, R. B. King, . F. Schaefer, H, III *J. Am. Chem. Soc.*, **2005**, *127*, 11564.
17. H. Wang, Y. Xie, R. B. King, H. F. Schaefer, , III *Inorg. Chem.*, **2006**, *45*, 5621.
18. H. Wang, Y. Xie, R. B. King, H. F. Schaefer, III *Organometallics*, **2007**, *26*, 1393.
19. X. Zhang, Q.-S. Li, Y. Xie, R. B. King, H. F. Schaefer, *Organometallics*, **2008**, *27*, 61.
20. A. D. Becke, *J. Chem. Phys*. **1993**, *98*, 5648.
21. C. Lee, W. Yang, R. G. Parr, *Phys. Rev*. *B* **1988**, *37*, 785.
22. A. D. Becke, *Phys. Rev*. *A* **1988**, *38*, 3098.
23. J. P. Perdew, *Phys. Rev*. *B* **1986**, *33*, 8822.
24. T. H. Dunning, *J. Chem. Phys*. **1970**, *53*, 2823.
25. S. *J.* Huzinaga, *Chem. Phys*. **1965**, *42*, 1293.
26. A. J. H. Wachters, *J. Chem. Phys.* **1970**, *52*, 1033.
27. D. M. Hood, R. M. Pitzer, H. F. Schaefer, *J. Chem. Phys.* **1979**, *71*, 705.
28. L. R. Byers, L. F. Dahl, *Inorg. Chem.* **1980**, *19*, 680.
29. F. R. Anderson, M. S. Wrighton, *Inorg. Chem*., **1986**, *25*, 112.
30. S. Gambarotta, C. Floriani, A. Chiesi-Viulla, C. Guastini, *J. Organometal. Chem.* **1985**, *296*, C6.
31. R. B. King, *Inorg. Chem.* **1966**, *5*, 2227*.*

STUDIA UNIVERSITATIS BABEŞ-BOLYAI, CHEMIA, LIII, 2, 2008

TEMPERATURE-INDEPENDENT LONGITUDINAL WAVES OBTAINED ON CARBON NANOTUBES WITH SPECIAL EMPHASIS ON THE TUBULAR ION-TRANSPORT

BEÁTA PELES-LEMLI[a], JÁNOS PELES-LEMLI[a], LÁSZLÓ KOLLÁR[b],
GÉZA NAGY[a], SÁNDOR KUNSÁGI-MÁTÉ[a]

ABSTRACT. The vibration properties of two representative types of achiral carbon nanotubes were investigated by temperature dependent MDs calculations. The changes of the diameters of SWCNTs in time were calculated using the distances between the two opposite atoms of the nanotube. Periodical changes of diameters of nanotube's cross-section ellipsoid were obtained in picosecond time-scale. Our results show that a longitudinal wave of conformation change travels along the longitudinal axis of the nanotube. A kind of travelling with 20 nm/ps speed pulsation could be observed of the elliptic cross section through a circular instant. This finding corresponds to the transport of ions or molecules in the nanotube, since these particles are preferred to be kept in the symmetric circle cross section of the nanotube.

Keywords: *carbon nanotubes, molecular and ion transport, Molecular Dynamics calculations*

INTRODUCTION

A single-walled carbon nanotube (SWCNT) consists of a graphene sheet rolled up to cylinder. The tubes are several nanometers in diameter and several microns in length. SWCNTs have a fascinating ability to encapsulate atoms, ions and molecules in their one-dimensional nanotube. Nowadays especially the ion [1] and molecule transports [2] in these nanoscale channels have gained increasing attention.

In this way, to optimize the practical performance of SWCNTs, more detailed knowledge about their physical and chemical properties is required, because their special properties, *e.g.* their one-dimensional form, make them highly attractive materials, even so the very complex behaviour of the transport skill hinders their wide-scale application. Our previous work, related to formation-dissociation dynamics of the calixarenes' host-guest complexes [3]

---

[a] *Department of General and Physical Chemistry, University of Pécs, Ifjúság 6,H-7624 Pécs, Hungary, e-mail: kunsagi@gamma.ttk.pte.hu*
[b] *Department of Inorganic Chemistry, University of Pécs, Ifjúság 6,H-7624 Pécs, Hungary*

shows an example that Molecular Dynamics (MDs) calculations are fruitful testing techniques to analyze the dynamic processes of aromatic molecules at molecular level. Accordingly, the vibrational properties of two representative types of carbon nanotubes are investigated by temperature dependent MDs calculations. The (4,4) and (7,0) SWCNTs of similar diameter sizes were studied. Part of the calculations are performed using GAUSSIAN 03 program package and the MDs investigations were carried out with HyperChem Professional 7 program package using MM+ forcefield approximation. The aim of this preliminary investigation was to get information how these vibrations could affect *(i)* the speed of the molecule and ion transport through these nanomaterials and *(ii)* the strength of π-π interaction taking part in the adsorption of packing organic molecules on the surface of carbon nanotubes.

RESULTS AND DISCUSSION

The changes of the diameters of SWCNTs in time were calculated using the distances between the two opposite atoms of the nanotube (Fig. 1). Periodical changes of diameters of nanotube's cross-section ellipsoid were obtained in picosecond time-scale.

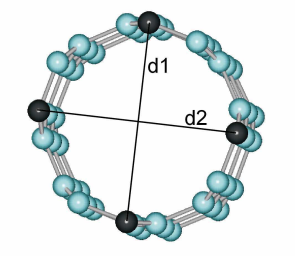

Figure 1. Periodical changes of diameters of nanotube's cross-section ellipsoid were calculated using the distances between the two opposite atoms of the nanotube

These conformation changes also affect the atomic vibrations orthogonal to the nanotube surface (Fig. 2), which property alone could affect the solubilization of nanotubes. One of the possible solubilization processes related to the noncovalent sidewall SWCNT functionalization with aromatic organic molecules [4]. The key features in the solubilization process is the π–π interactions between the aromatic ‘packer’ compounds and the SWCNT [5]. On the one hand the strength of the π–π interactions depends on the size of the aromatic moiety of the packer molecule consideration the curvature of the SWCNT surface and the shapes of the interacting ring systems. However, our results suggest, that packer molecules of more flexible structure can be attached stronger to the SWCNT, because the periodic changes of nanotube geometry can inhibit the fit of the packer molecules to the nanotube's surface in a wide time scale.

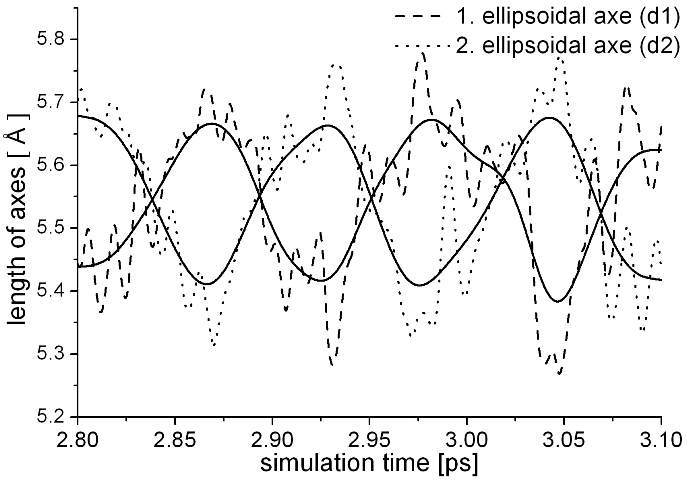

Figure 2. The variation of the d1 and d2 diameters as the function of time

Interestingly, our results show that a longitudinal wave of the conformation change (based on the diameters' changes described above) travels along the longitudinal axis of the nanotube. The speed of this wave can be derived from the two characteristic data of nanotube motion: *i)* from the distance *d* between two ellipsoidal cross sections of nanotube with same orientation and *ii)* from time constant *t* of vibration of the cross section of nanotube. (In other words: *d* reflects the distance that the wave takes until the time constant *t* of vibration of the cross section.) Therefore, the speed of the wave can be derived as the ratio of *d* and the time constant *t*. The speed determined on such way is 20 (±1.2) nm/ps. This speed pulsation seems to be temperature independent in the investigated temperature range (Fig. 3). This finding corresponds to the transport of ions and small ionic and neutral molecules.

The work of Sholl et al. [6] shows that the energy transfer between the nanotubes and the diffusing methane molecules highly affect the diffusion coefficient. Our results highlighted that the energy transfer also depends on the geometry changes of the SWCNT. We have found, that the longitudinal wave of the conformation change travels along the longitudinal axis of the nanotube at the rate of 20 nm/ps. Considering this result together with the diameter of the investigated SWCNTs, the speed of the investigated wave generated by the diameter changes of SWCNT is about 4.6×10^{-1} cm^2 s^{-1}, which value is in the range of the calculated diffusion coefficients of Sholl et al. [6].

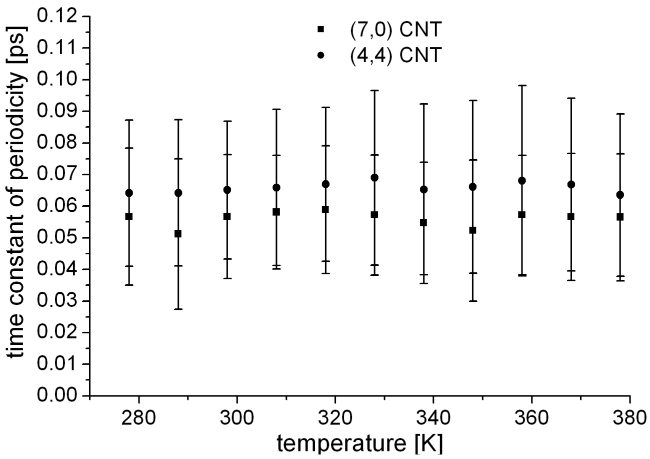

Figure 3. Temperature dependence of the speed of longitudinal waves obtained along the carbon nanotubes

CONCLUSIONS

Nevertheless the two representative types of achiral single-walled carbon nanotubes have more important different physical and chemical properties. It was shown that the investigated semiconductor zigzag (7,0) and metallic armchair (4,4) SWCNTs have no significant difference in their vibration dynamics properties in the studied temperature range of 278-378 K. A longitudinal wave of conformation change travels along the longitudinal axis of the nanotube at a temperature independent speed pulsation of 20 nm/ps in the investigated temperature range. These results support that the pulsation of the nanotube can control the transfer of any kind of particles whose shape fit to an actual conformation of the nanotube wall. As a consequence, the transfer of these particles will be temperature independent in the examined temperature range. This finding might be is applicable to the wide-scale of electrochemical research.

ACKNOWLEDGMENTS

S-K.-M. whishes to thank the Hungarian Academy of Sciences for a János Bolyai Fellowship. Parts of calculations were performed on SunFire 15000 supercomputer located in the Supercomputer Centre of the Hungarian National Infrastructure Development Program Office.

REFERENCES

1. J.W. Kang, K.R. Byun, J.Y. Lee, S.C. Kong, Y.W Choi, H.J. Hwang, *Physica E*, **2004**, *24*, 349.
2. A. Kalra, G. Hummer, S. Garde, *J. Physical Chemistry B*, **2004**, *108*, 544.
3. B. Peles-Lemli, J. Peles-Lemli, I. Bitter, L. Kollár, G. Nagy, S. Kunsági-Máté, *J. Inclusion Phenomena and Macrocyclic Chemistry*, **2007**, *59(3-4)*, 251.
4. N. Nakashima, *Science and Technology of Advanced Materials*, **2006**, *7*, 609.
5. L.M.Woods, S.C. Badescu S.C., T.L. Reinecke, *Physical Rewiev B*, **2005**, *75*, 155415.
6. H. Chen, D.S. Sholl, *J. Physical Chemistry B*, **2006**, *110*, 1971.

STUDIA UNIVERSITATIS BABEŞ-BOLYAI, CHEMIA, LIII, 2, 2008

GRID-BASED CONFORMATIONAL SAMPLING

BENJAMIN PARENT[a], ALEXANDRU TANTAR[b], NOUREDINE MELAB[b], EL-GHAZALI TALBI[b], DRAGOS HORVATH[c,*]

ABSTRACT. Computational simulations of conformational sampling in general, and of macromolecular folding in particular represent one of the most important and yet one of the most challenging applications of computer science in biology and medicinal chemistry.

This paper presents a massively parallel GRID-based conformational sampling strategy, exploring the extremely rugged energy response surface in function of molecular geometry, in search of low energy zones through phase spaces of hundreds of degrees of freedom.

We have generalized the classical island model deployment of Genetic Algorithms (GA) to a "planetary" model where each node of the GRID is assimilated to a "planet" harboring quasi-independent multi-island simulations using a hybrid GA.

Although different "planets" do not communicate to each other -thus minimizing inter-CPU exchanges on the GRID- each new simulation will benefit from the preliminary knowledge of already visited geometries, located on the dispatcher machine, and which are disseminated to any new "planet". This "panspermic" strategy allows new simulations to be conducted such as to either be attracted towards an apparently promising phase space zone (biasing strategies, intensification procedures) or to avoid already in-depth sampled (tabu) areas.

Successful all-atom folding of mini-proteins typically used in benchmarks (the Trp cage 1L2Y and the Trp zipper 1LE1) has been observed, although the reproducibility of these highly stochastic simulations in huge problem spaces is still in need of improvement.

Keywords: *molecular modeling, conformational sampling, protein folding simulations, genetic algorithms, massively parallel computing, molecular force fields*

INTRODUCTION

The prediction of 3D shapes of molecules on hand of their connectivity (the so-called *Conformational Sampling, CS*) is a widely addressed, central problem in structural biology and drug design[1]. There are yet no general approaches able to enumerate, for an arbitrary (macro)molecule, the most

---

[a] *Institut Suprieur d'Electronique et du Numérique; 41, Bd. Vauban, 59000 Lille, FR*

[b] *Laboratoire d'Informatique Fondamentale, Cité Scientifique, 59655 Villeneuve d'Ascq, FR*

[c] *Laboratoire d'InfoChimie, Univ. Louis Pasteur, 4, rue Blaise Pascal, 6700 Strasbourg, FR*

* *Corresponding author: horvath@chimie.u-strasbg.fr*

stable molecular geometries adopted in solution. Several proofs of the NP-completeness of such a problem have been proposed on hand of different models [2, 3], while protein chemists are well aware of the Levinthal paradox [4]. The reformulation in terms of an energy landscape [5], where the energy is a force field-based [6, 7] function of internal coordinates (in this case, dihedral angles around the considered rotatable bonds), enables to attack the problem in the framework of function optimization. Energy minima then correspond to the populated geometries of the molecule. The extreme ruggedness of the response hypersurface causes any deterministic optimization attempt to get stuck in local, most likely irrelevant optima and imposes the use of stochastic sampling procedures.

The ability of GAs to deal with a set of solutions while deriving profit of an intrinsic stochastic behavior in addition to the recombination principle, makes them a suited tool for challenging highly multimodal and highly dimensional problems [8]. The high computational costs, on one hand, and the straightforwardness of parallel deployment strategies for genetic algorithms, on the other, make this problem an ideal candidate for GRID computing. In the following we report, after a short introduction of the hybrid island model [9], a first successful deployment strategy on the parallel GRID[1] context, the "planetary'" model.

The hybrid GA deployed on the "planets" (nodes) of the GRID operates on the degrees of freedom associated to the rotations around interatomic single bonds, so that a chromosome represents the vector of torsional angles associated to rotatable bonds. Certain peculiarities of the sampling problem ask for hybridizations [9] of the GA with other optimization procedures (conducting "Lamarckian" local optimizations to repair local clashes in what would otherwise represent stable conformers, allow for "directed" mutations, permitting the other degrees of freedom to adjust in response to the random shift applied to the mutated chromosome locus, introduce population diversity management criteria, biased random distributions for each degree of freedom, etc).

In the planetary approach, a dispatcher script attempts to deploy island models on as many nodes (planets) as requested, if it can find the resources on the GRID. Once an island model is completed according to the locally specified termination criteria, the island model pilot script sends the locally sampled results back to the dispatcher, which will join them to the "Universal" pool of solutions. Liberation of a node will prompt the dispatcher to restart an island model there, until a total (user-specified) number of sets of results were successfully retrieved, or until the latest (user-defined) N retrieved results failed to contain any fitter solutions. The behavior of each island model is controlled by a set of operational parameters dictated by the dispatcher, which actively tries to optimize these in order to achieve better sampling capacity of the further runs.

---

[1] supported by the French GRID5000 initiative (www.grid5000.fr) and the Agence Nationale de la Recherche

A key element of our deployment strategy is “panspermia”, so entitled after the hypothesis that life on Earth might have been seeded by microorganisms from space: the dispatcher may randomly pick a subset of the already visited solutions from the “Universal” pool and “seed” any newly started CS run. The latter may use the provided sample to specify these as tabu zones [10] -forcing the exploration of other phase space zones (default exploratory runs)- or to replace the random initialization of chromosomes by cross-over products of these “ancestors”, thus allowing an in-depth exploration of promising phase space regions (intensification runs).

Unfortunately, the ruggedness of the energy landscape is such that near-native structures (according to geometric criteria) may nevertheless display high energies and fail to rank among the populated states. A specific “intensification” scheme for the GA, [11] allowing the fine exploration of limited phase space zones has therefore been designed. Its initial populations are not random, but loaded with previously sampled geometries representing a same global fold, in search for states of similar overall geometry but lower energy.

Heavily visited phase space zones, where the deepest zonal optimum has been (expectedly) sampled, will be declared tabu areas in future exploratory runs. Any solution close, according to a given similarity metric and similarity cut-off, to a tabu chromosome, will be assigned a low fitness score. The choice of the similarity metric and cut-off (see [11] for details) is paramount: too broad taboo areas may block the access to unexplored deeper local minima in the neighborhood.

The key challenge of an optimal panspermic strategy is to decide at which point chromosomes have served enough in intensification searches, and therefore should be declared tabu. A too early decision in this sense may prematurely block the discovery of deep energy wells, while a too late one translates in wasted computer time. Common sense might suggest that intensification should be applied only to chromosomes of reasonably low energies, but in practice it is unclear what “reasonably low” is supposed to mean: intensification may dramatically lower intramolecular strain.

RESULTS AND DISCUSSION

Up-to-date attempts to use the planetary model led to successful folding experiments of the Trp cage 1L2Y [12] (α-helix) and Trp zipper 1LE1 [13] (β-sheet), in a matter of few days, using only a small subset (20-30 nodes) of GRID5000.

α-helices are structural elements that fold quickly in solution, being stabilized by local, energetically favorable hydrogen bonds. This situation is well suited for GA-based sampling: a helix turn is controlled by 6 degrees of freedom only, i.e. may quite easily emerge by hazard in a chromosome. Being stabilized by internal hydrogen bonds, this structural element is readily inherited, until a favorable cross-over may couple two spontaneously emerged helix loops together. Accordingly, the planetary model has successfully and reproducibly discovered, as shown in Figure 1, geometries that are very close to the native 1L2Y fold reported in literature.

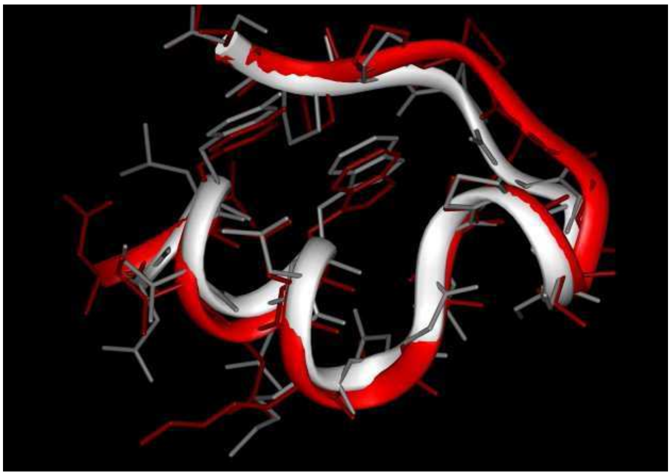

Figure 1. Best ranked (lowest energy) conformer found by the planetary model for 1L2Y (red) overlayed to native 1L2Y geometry (white). Heavy atom RMSD is of 1.8 Å

By contrast, although the Trp zipper has only 53 degrees of freedom, it is nevertheless more difficult to fold computationally than 1L2Y. The main reason is its β-hairpin structure, where stabilizing hydrogen bonds stem from topologically remote pairs of aminoacids. The β-sheet zipper is a cooperative element: it gains stability only when fully structured: chromosomes displaying partly folded sheets will not benefit from stabilization, *i.e.* do not have any obvious evolutionary advantage. This notwithstanding, correctly folded protein backbones have been reproducibly obtained by planetary model-based simulations. In rare cases (2 out of several tens), the simulation actually returned a perfect replica of the experimental fold, both in terms of backbone and side chain orientations. This calculated geometry (Figure 2) was also shown to be the most stable of all the ever visited 1LE1 conformers.

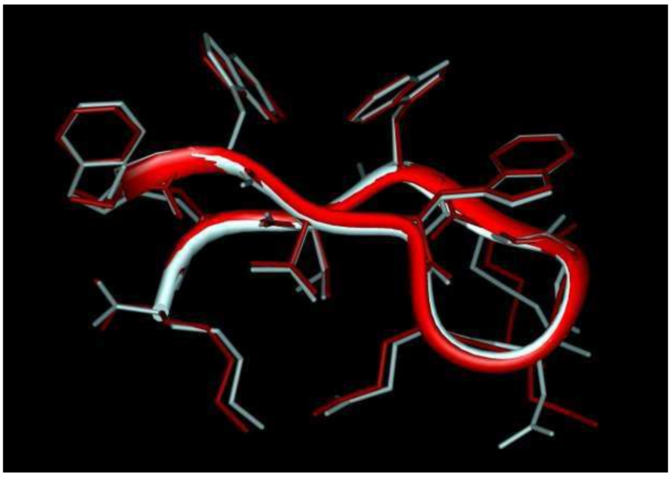

Figure 2. Some simulations lead to the discovery of the exact native geometry of 1LE1

Typical simulations, however, return geometries like in Figure 3, where the backbone is correctly folded but side chains are misplaced. The alternative side chain interactions make physico-chemical sense: (aromatic stacking, like in the native geometry). The computed conformer is not obviously wrong: it may actually correspond to some less populated species which escapes detection by state-of-the-art experimental methods. However, its computed energy is significantly higher than the one of the native state and, unfortunately, also higher than the one of misfolded structures: it was ranked as the 79th most stable geometry out of several hundreds of thousands.

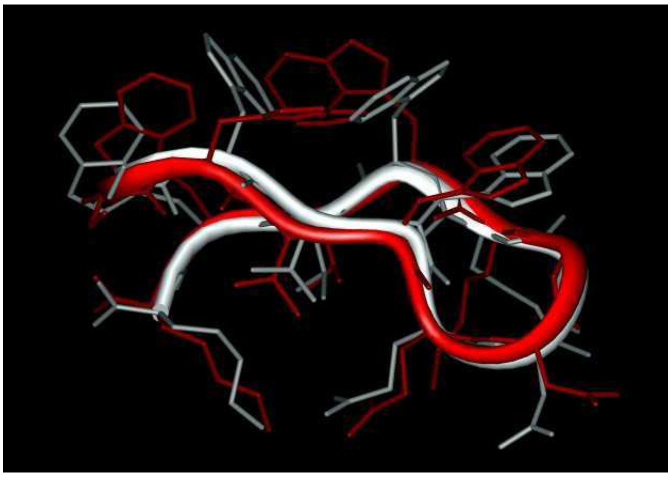

Figure 3. Typical 1LE1 folding behaviour: *almost* native structures differing from the latter only with respect to their side chain placement, are readily found.

CONCLUSIONS

The herein presented “planetary” conformational sampling approach showed some promising first results – correct folding of helical peptides, and occasional convergence towards the native geometry of β-sheet peptides. However, the “panspermic” strategy at the core of the planetary approach needs further refinement, for the failure to systematically converge towards the native 1LE1 geometry may be ascribed to an overhasty setting of tabu areas in the neighborhood of almost native geometries, with a correct backbone fold but wrong side chain orientations. Such tabu zones are responsible, in addition to the intrinsic ruggedness of the energy landscape, for the failure of the method to successfully move from these relatively energy-rich almost correct folds to the low energy native structure.

REFERENCES

1. J. N. Onuchic, P.G. Wolynes, *Curr. Op. Struct. Biol.*, **2004**, *14*, 70.
2. P. Crescenzi, D. Goldman, C.H. Papadimitriou, A. Piccolboni, M. Yannakakis, *J. Comp.Biol.*, **1998**, *5*, 423.
3. R. Unger, J. Moult, *J. Mol. Biol.*, **1993**, *231*, 75.
4. C. Levinthal, in *Mossbauer Spectroscopy in Biological Systems.*, University of Illinois Press, Chicago, Editon edn., 1969, pp. 22.
5. D. J. Wales, T.V. Bogdan, *J. Phys. Chem.*, **2006**, *110*, 20765.
6. A. T. Hagler, E. Huler, S. Lifson, *J. Am. Chem. Soc.*, **1974**, *96*, 5319.
7. A. T. Hagler, S. Lifson, *J. Am. Chem. Soc.*, **1974**, *96*, 5327.
8. J. Holland, *Adaptation in Natural and Artificial Systems.*, University of Michigan Press, Ann Arbor, 1975.
9. B. Parent, A. Kökösy, D. Horvath, *Soft Computing*, **2007**, *11*, 63.
10. F. Glover, J.P. Kelly, M. Laguna, *Computers and Operations Research*, **1995**, *22*, 111.
11. B. Parent, A. Tantar, N. Melab, E.-G. Talbi, D. Horvath, IEEE Congress on Evolutionary Computation, CEC 2007, Singapore, http://www.ieeexplore.ieee.org/iel5/4424445/4424446/04424484.pdf?tp=&arnumber=4424484&isnumber=4424446, 2007.
12. J. W. Neidigh, R. M. Fesinmeyer, N. H. Andersen, *Nature Struct. Biol.*, **2002**, *9*, 425.
13. A. G. Cochran, N.J. Skelton, M.A. Starovasnik, *Proc. Natl. Acad. Sci. USA*, **2001**, *98*, 5578.

STUDIA UNIVERSITATIS BABEŞ-BOLYAI, CHEMIA, LIII, 2, 2008

BASIC TESSELLATIONS IN NANOSTRUCTURES

MIRCEA V. DIUDEA[*]

ABSTRACT. Basic tessellations in nanostructures, like the polyhex (6,3) and pattern, encountered in nanotubes and tori as well as the fullerene coverings derived from the Platonic solids can be performed by two main procedures, implemented in three original software programs developed at the TOPO Group Cluj: the cut procedure, suitable for tubular structures covering and the map operations, for spherical structures. Correspondence between Cluj-like and the classical notation of tubular structures is clearly demonstrated. Parameters of the transformed networks are given in terms of the primitive lattice vectors and original cage covering. Electronic structure of at the simple π-Hückel accounts for the metallic or insulating behavior of tubular structures. Covering criteria for metallic character in polyhex tori are derived from the network parameters. Formulas for the iterative operations on maps of vertex degree three are presented.

INTRODUCTION

Covering a surface by various polygonal or curved regions is an ancient human activity. It occurred in house building, particularly in floor, windows and ceiling decoration. There were well known three regular Platonic tessellations (*i.e.*, coverings by a single type face and a single vertex degree): (4,4), (6,3) and (3,6). The Greek and Roman mosaics were very appreciated in this respect.

Covering is nowadays a mathematically founded science.[1-4] Covering modification is one of the ways in understanding chemical reactions occurring in nanostructures, particularly in carbon allotropes. Nanostructure modeling necessarily involves the embedding of a polygonal lattice in a given 3D surface *S*. Such a “combinatorial” surface is called a map *M*. Analytical formulas, for generating a smooth surface, can be found in Mathematical recipes, available on internet. The coordinates of the lattice points are obtained by partitioning *S*, either by dedicated algorithms or by simply drawing vertices and edges on display, with the aid of some builders to switch from 2D to 3D. Another way uses templates, *e.g.*, unit blocks with a prescribed spatial arrangement. The TOPO Group Cluj has developed three main software programs TORUS [5] CageVersatile [3] (CVNET) and JSCHEM [6].

---

[*] *Faculty of Chemistry and Chemical Engineering, “Babeş-Bolyai” University, 400028, Cluj, Romania*

SQUARE (4,4) LATTICE

The embedding of the (4,4) net is made by circulating a *c*-fold cycle, circumscribed to the toroidal tube cross-section, along the cylinder or around the large hollow of the torus. The subsequent *n images* of *c*-fold cycle, equally spaced are joined with edges, point by point, to form a polyhedral cylinder/ torus tiled by a tetragonal pattern. Twisted, chiral, (4,4) tori can be generated by the following two procedures: [4,7] (1) twisting the horizontal layer connections (Figure 1a) and (2) twisting the vertical layer (offset) connections (Figure 1b).

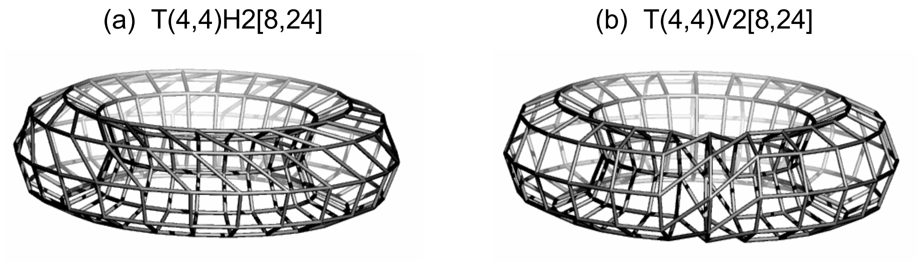
(a) T(4,4)H2[8,24]

(b) T(4,4)V2[8,24]

Figure 1. An H-twisted (a) and a V-twisted (b) embedding of the (4,4) net.

POLYHEX (6,3) NETWORK

To obtain the (6,3) tessellation,[1,4,7] each second edge of the (4,4) net has to be cut off. Two isomeric embeddings can be defined in the torus. Two topologically distinct tori are obtained by the TORUS program: T(6,3)H/Z[*c*,*n*] and T(6,3)V/A[*c*,*n*] and they correspond to two different classes of aromatic chemical compounds, phenacenes and acenes, respectively. The H-embedding is obtained when the cut edges lye horizontally (*i.e.*, perpendicular to the Z axis of the torus). It is also called "zigzag" Z, by the tube cross-section shape. The V-embedding results when the cut edges lye vertically (*i.e.*, parallel to the Z axis of the torus). It is also called "armchair" A, by the tube cross-section aspect. The name of such tori is a string of characters including the tiling, type of embedding and the tube dimensions [*c*,*n*].

By performing a cross-section on a polyhex torus (or by using the cylinder to embed a (4,4) net leading ultimately to the (6,3) pattern) and next optimizing, by a Molecular Mechanics procedure, the generated polyhex tubes and tori look like in Figure 2. The objects in these examples represent non-chiral structures.

Each of the twisting of the (4,4) tori (Figure 1) lead to four classes [7] of twisted tori: (i) H-twist, H-cut HH*t*[*c*,*n*]; (ii) H-twist, V-cut, HV*t*[*c*,*n*]; (iii) V-twist, H-cut, VH*t*[*c*,*n*]; and (iv) V-twist, V-cut, VV*t*[*c*,*n*]. The type of cutting will dictate the type of embedding and, ultimately, the shape of objects. Conversely, the type of twisting is involved in the π-electron structure of polyhex tori. Figure 3. illustrates some (non-optimized) twisted polyhex tori.

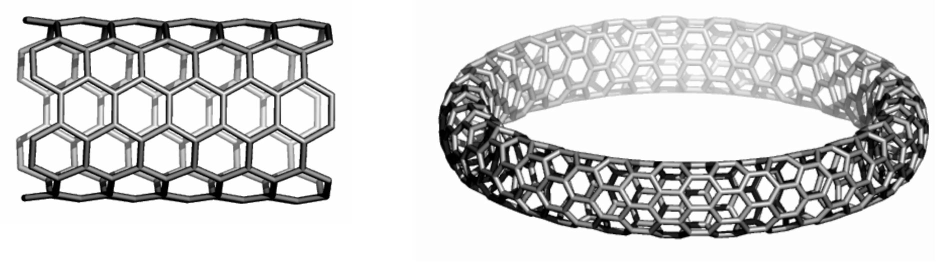

(a) Tu(6,3)V/A[12,12]; *v* = 144

(b) T(6,3)H/Z[12,50]; *v* = 600

Figure 2. The (6,3) covering in the cylindrical (a) and toroidal (b) embedding, respectively.

The twist number *t* is just the deviation (in number of hexagons) of the chiral (*i.e.*, rolling-up) vector to the zigzag line, in the graphite sheet representation [8-11] Accordingly, a torus can be drawn as an equivalent planar parallelogram, involving two tubes: one tube is built on the rolling-up vector *R* (Figure 3.7), which, in terms of the primitive graphite lattice vectors, is written as:

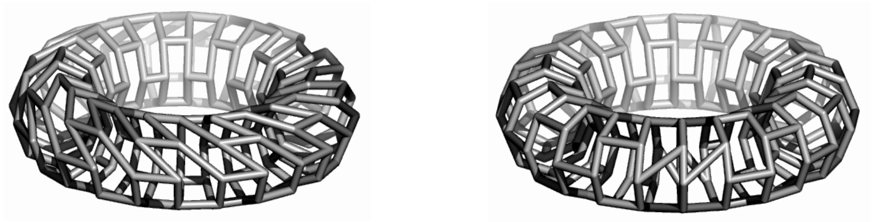

T(6,3)HH2[8,24]

T(6,3)VH2[8,24] (offset)

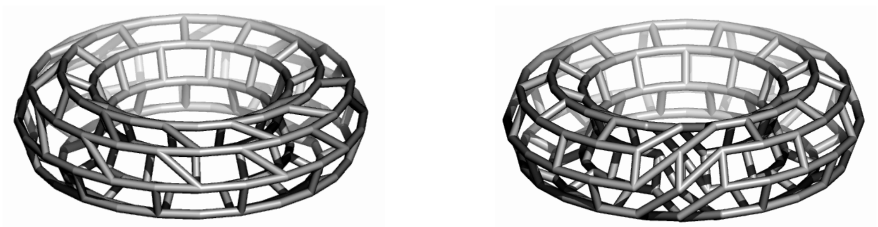

T(6,3)HV2[8,24]

T(6,3)VV2[8,24] (offset)

Figure 3. The four classes of twisted polyhex tori (non-optimized).

$$R = ka_1 + la_2 \tag{1}$$

The second tube is formally defined on the translating vector *T*:

$$T = pa_1 + qa_2 \tag{2}$$

For a given torus, the first tube can be identified by cutting the object across the tube while the second one results by cutting it around the large hollow. Anyway, a four integer parameter description (*k*,*l*,*p*,*q*) can be written. The coordinates of THH4[14,6] torus depicted in Figure 4 are: [7] (5, -4, 3, 3). Note that this representation is not unique and is reducible to three parameter notation, theorized by Kirby *et al* [9,12].

Correspondence between our notation for tubes (TUX*t*[*c*,*n*]) and tori (TX*t*[*c*,*n*]) and that in two (*k*,*l*) and four (*k*,*l*,*p*,*q*) integers notation are given in Tables 1 and 2, respectively.

Table 1.

Correspondence between the TUX*t*[*c*,*n*] and (*k*,*l*) notation.

	Tube X*t*	(*c*,*t*); (*k*,*l*)	Tube (*k*,*l*)
1	H	*c*=2*k*; *t*=*l*=0	(*c*/2,0); Z
2	HH*t*	*c*=*k*+2*l*; *t*=*k*; *l*=(*c*-*t*)/2	[*t*,(*c*-*t*)/2]
3	HV*t*	*c*=*k*+*l*; *t*=*k*; *l*=*c*-*t*	[*t*,(*c*-*t*)]
4	V	*c*=2*k*; *t*=*l*=0	(*c*/2,*c*/2); A

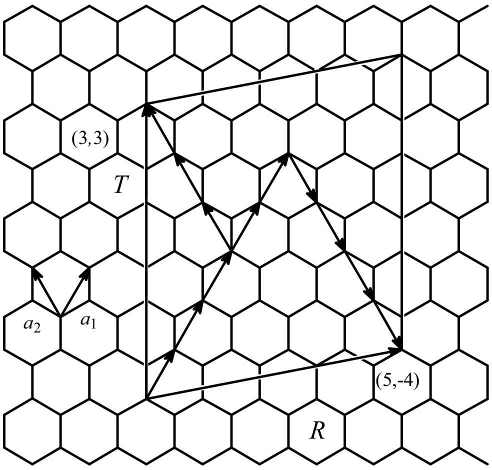

Figure 4. Representation of the torus THH4[14,6] by an equivalent parallelogram defining two tubes: one defined on the rolling-up vector *R* (with integer coordinates (*k*,*l*)) and the other on the translating vector *T* (given by the pair (*p*,*q*)). The four parameter specification of the depicted torus is (5, -4, 3, 3).

Table 2.

Correspondence between the TX*t*[*c*,*n*] and (*k*,*l*,*p*,*q*) notation.

	Torus X*t*	Tube *R*	Tube *T*	Torus (*k*,*l*,*p*,*q*)*	*v*
1	H	H/Z	V/A	$(c/2, -c/2, n/2, n/2)$	$2(kq - lp) = cn$
2	V	V/A	H/Z	$(c/2, c/2, n/2, -n/2)$	$2(lp - kq) = cn$
3	HH*t*	HH (tw)	V/A	$[(c-t)/2, -t, n/2, n/2]$	$2(2kq - lp) = cn$
4	HV*t*	HV (tw)	H/Z	$[(c+t)/2, (c-t)/2, n/2, -n/2]$	$2(lp - kq) = cn$
5	VH*t* (offset)	H/Z	HV (tw)	$[c/2, -c/2, (n+t)/2, (n-t)/2]$	$2(kq - lp) = cn$
6	VV*t* (offset)	V/A	HH (tw)	$[c/2, c/2, (n-t)/2, -t)]$	$2(2lp - kq) = cn$

* First pair (*k*,*l*) denotes the rolling-up vector *R* while last pair (*p*,*q*) specifies the translating vector *T*. The representation (*m*,-*m*) = (*m*,0), is an H/Z-tube while (*m*,*m*) is a V/A-tube.

π-ELECTRONIC STRUCTURE OF POLYHEX TORI

In the Spectral Theory, at the simple π-only Hückel [13] level of theory, the energy of the i^{th} molecular orbital $E_i = \alpha + x_i\beta$ is evaluated by calculating the solutions x_i of the characteristic polynomial *Ch*(*G*,*x*) or the eigenvalues of the adjacency matrix associated to the molecular hydrogen depleted graph.

The π-electronic shells of neutral graphitic objects are classified [14,15] function of their eigenvalue spectra, as *closed*, when $x_{v/2} > 0 \geq x_{v/2+1}$ or *open*, when the HOMO and LUMO molecular orbitals are degenerate, $x_{v/2} = x_{v/2+1}$.

The *metallic* character involves the existence of a zero HOMO-LUMO gap (a particular case of the open shell) and the degeneracy of some non-bonding orbitals [16] (NBOs) favoring the spin multiplicity, cf. the Hund rule. In polyhex tori, the metallic behavior is ensured by *four* NBOs, also present in the graphite sheet. The gap (in β units) is taken as the absolute value of the difference $E_{\mathrm{HOMO}} - E_{\mathrm{LUMO}}$. Table 3 gives the lattice [*c*,*n*] criteria (in terms of our notation) for metallic shell in (6,3) tori of various types.

Table 3.

Covering criteria for metallic character in polyhex tori

	Torus	Metallic
	Non-Twisted	
1	H/Z[*c*,*n*]	0 mod (*c*,6)
2	V/A[*c*,*n*]	0 mod (*n*,6)
	H-Twisted	

3	HH*t*[*c*,*n*]	0 mod (*c*,6)
4	HV*t*[*c*,*n*]	0 mod (*n*,6) 0 mod(*t*,6)
	V-Twisted	
5	VH*t*[*c*,*n*]	0 mod (*c*,6) 0 mod (*t*,6)
6	VV*t*[*c*,*n*]	0 mod (*n*,6)

OPERATIONS ON MAPS

Modifying a covering is one of the ways in understanding chemical reactions occurring in nanostructures, particularly in carbon allotropes [17-20].

A map *M* is a combinatorial representation of a (closed) surface [21]. Let us denote in a map: *v* – the number of vertices, *e* - the number of edges, *f* – the number of faces and *d* – the vertex degree. A subscript “0” will mark the corresponding parameters in the parent map. The famous EULER (1758) formula: [22,23]

$$v - e + f = \chi(M) = 2(1 - g) \tag{3}$$

with χ being the Euler *characteristic* and *g* the genus [24] of a graph is useful for checking the consistency of an assumed structure. Positive/negative χ values indicate positive/negative curvature of a lattice.

Some geometrical-topological transformations, called operations on maps, are used to relate parents and transformed associate graphs of nanostructures. In this respect, operations such as: dualization *Du*, medial *Me*, truncation *Tr*, polygonal P_r capping or Snub Sn, are well known. Among the five Platonic solids, Tetrahedron is self-dual, and the remainders form dual pairs: Cube-Octahedron and Dodecahedron-Icosahedron (Figure 5).

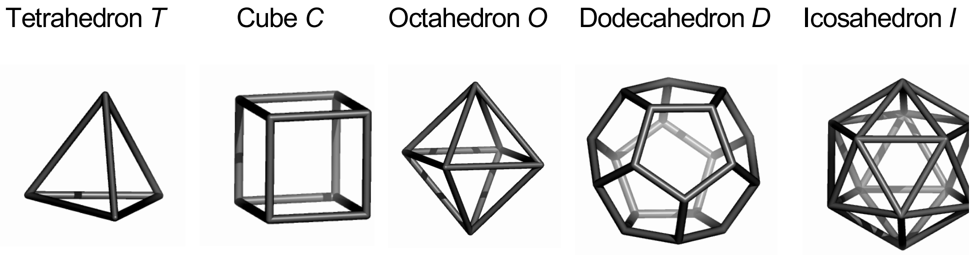
Tetrahedron *T* Cube *C* Octahedron *O* Dodecahedron *D* Icosahedron *I*

Figure 5. The five Platonic polyhedra.

Some other operations can be derived ac combinations of the simplest ones. In the following, three of the most important composite operations on maps are presented.

Leapfrog *Le*. Leapfrog (*tripling*) is a composite operation [25-32] that can be written as:

$$Le(M) = Du(P_3(M)) = Tr(Du(M)) \tag{4}$$

A sequence of stellation-dualization rotates the parent *s*-gonal faces by π/s. Leapfrog operation is illustrated, on a pentagonal face, in Figure 6.

A bounding polygon, of size $2d_0$, is formed around each original vertex. In the most frequent cases of 4- and 3-valent maps, the bounding polygon is an octagon and a hexagon, respectively.

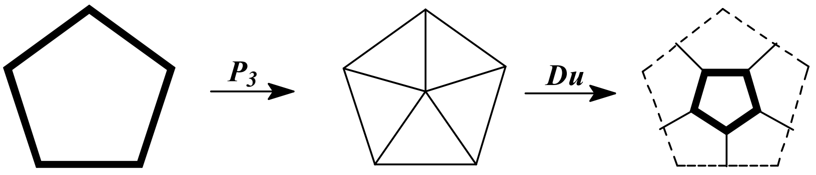

Figure 6. The Leapfrog *Le* operation on a pentagonal face

The number of vertices in Le(M) is d_0 times larger than in the original d_0 regular map M, irrespective of the tessellation type. The complete transformed map parameters are:

$$Le(M){:}\quad v = s_0 f_0 = d_0 v_0\,;\quad e = 3e_0\,;\quad f = v_0 + f_0 \tag{5}$$

Note that in *Le*(*M*) the vertex degree is *always* 3, as a consequence of the involved triangulation P_3. In other words, the dual of a triangulation is a *cubic net* [21]. A nice example of using *Le* operation is: *Le*(Dodecahedron) = Fullerene C_{60} (Figure 7). The leapfrog operation can be used to insulate the parent faces by surrounding bounding polygons.

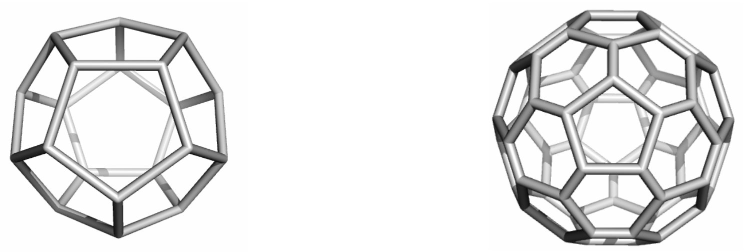
Dodecahedron *D*; *v* = 20

Fullerene C_{60} ; *v* = 60

Figure 7. Realization of *Le* operation

Chamfering *Q*. Chamfering (quadrupling) [30-33] is another composite operation, written as the sequence:

$$Q(M) = RE(Tr_{P_3}(P_3(M))) \tag{6}$$

where *RE* denotes the (old) edge deletion (dashed lines, in Figure 8) in the truncation Tr_{P3} of each central vertex of the P_3 mapping. The *Q* operation leaves unchanged the initial orientation of the polygonal faces.

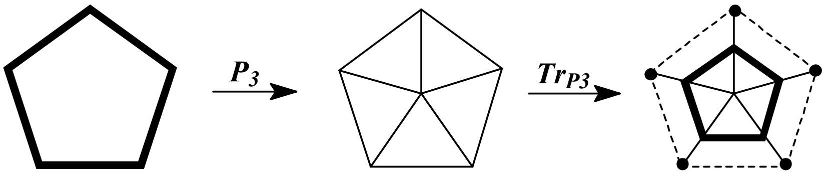

Figure 8. The Quadrupling *Q* operation on a pentagonal face.

The vertex multiplication ratio in a Q transform is d_0+1 irrespective of the parent map tessellation. The complete transformed parameters are:

$$Q(M):\ v = (d_0 + 1)v_0\,;\ e = 4e_0\,;\ f = f_0 + e_0 \tag{7}$$

Q operation involves two π/*s* rotations, so that the initial orientation of the polygonal faces is preserved. Note that, because of preserving the old vertices, *Q*(*M*) is, in general, non-regular; only in case of a 3-valent *M*, *Q*(*M*) is a 3-regular graph and vertex multiplication is 4 (from which the name *quadrupling* is derived. *Q* insulates the parent faces always by hexagons. An example of this operation is: *Q* (Dodecahedron) = Fullerene C_{80} (Figure 9).

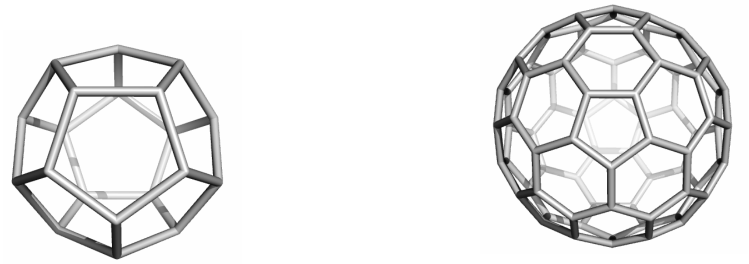
Dodecahedron *D*; *v* = 20

Fullerene C_{80} ; *v* = 80

Figure 9. Realization of *Q* operation

Capra *Ca.* Capra operation is a composite operation that can be written as a sequence of simple operations: [1,4,7,34-38]

$$Ca(M) = Tr_{P_5}(P_5(M)) \tag{8}$$

with Tr_{P5} meaning the truncation of new, face centered, vertices introduced by P_5 pentagonal mapping (Figure 10).

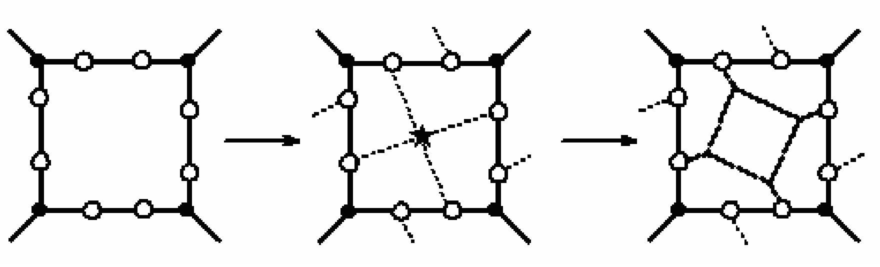

Figure 10. The Capra operation on asquare face.

The nuclearity of the Goldberg (1937) polyhedra [33] (related to the fullerenes) is given by the parameter:

$$m = (a^2 + ab + b^2);\ a \geq b;\ a + b > 0 \tag{9}$$

which is the multiplication factor $m = v/v_0$: in a 3-valent map, *Le* ((1,1); $m = 3$; *Q* ((2,0); $m = 4$ and *Ca*((2,1); $m = 7$. The m factor was used since the ancient Egypt for calculating the volume of truncated pyramid, of height h: $V = mh/3$.

Ca insulates any face of *M* by its own hexagons, which are not shared with any old face. It is an intrinsic chiral operation [37] (it rotates the parent edges by π/(3/2)*s*. Since pentangulation of a face can be done either clockwise or counter-clockwise, it results in an enantiomeric pair of objects: $Ca_S(M)$ and $Ca_R(M)$, with the subscript *S* and *R* given in terms of the *sinister*/*rectus* stereochemical isomerism.

The vertex multiplication ratio in the *Ca* operation is $2d_0 + 1$ irrespective of the original map tiling. The transformed map parameters are shown in the following relations:

$$Ca(M):\ v = v_0(2d_0 + 1);\ e = 7e_0;\ f = f_0(s_0 + 1) = 2e_0 + f_0 \tag{10}$$

The iterative n-time operating (on maps with vertex degree $d_0 = 3$) leads to the following transformed lattice parameters: [4,7]

$$v_n = 7^n v_0;\ \ e_n = 7^n e_0;\ \ f_n = f_0(s_0(7^n - 1)/6 + 1) \tag{11}$$

An example of molecular realization of *Ca* operation (applied on the Dodecahedron) is the chiral fullerene C_{140} (Figure 11).

C_{140}

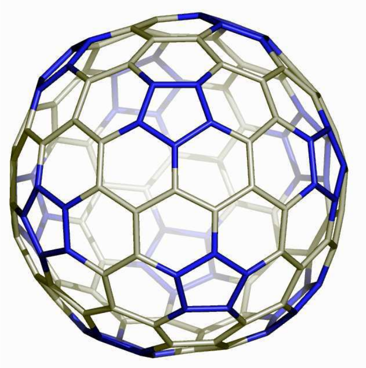

Figure 11. Realization of the Capra *Ca* operation

REFERENCES

1. M. V. Diudea, Covering forms in nanostructures, *Forma* (Tokyo), **2004**, *19*, 131.
2. M. V. Diudea and P. E. John, A. Graovac, M. Primorac, and T. Pisanski, *Croat. Chem. Acta*, **2003**, *76*, 153.
3. M. Stefu and M. V. Diudea, *CageVersatile* 1.3, "Babes-Bolyai" University, 2003.
4. M. V. Diudea and Cs. L. Nagy Cs. L., *Periodic nanostructures*, Springer, Chap. 6, 2007.
5. M. V. Diudea, B. Parv and O. Ursu, TORUS, "Babes-Bolyai" University, 2001.
6. Cs. L. Nagy, M. V. Diudea, JSCHEM, "Babes-Bolyai" University, 2004.
7. M. V. Diudea, Ed., *Nanostructures, novel architecture*, NOVA, N. Y., 2005.
8. A. Ceulemans, L. F. Chibotaru, and P. W. Fowler, *Phys. Rev. Lett.*, **1998**, *80*, 1861.
9. E. C. Kirby, R. B. Mallion, and P. Pollak, *J. Chem. Soc. Faraday Trans.*, **1993**, *89*, 1945.
10. S. A. Bovin, L. F. Chibotaru, and A. Ceulemans, *J. Molec. Catalys.*, **2001**, *166*, 47.
11. N. Hamada, S. Sawada, and A. Oshiyama, *Phys. Rev. Lett.*, **1992**, *68*, 1579.
12. E. C. Kirby and P. Pollak, *J. Chem. Inf. Comput. Sci.*, **1998**, *38*, 66.
13. E. Hückel, *Z. Phys.*, **1931**, *70*, 204.
14. P. W. Fowler, *J. Chem. Soc., Faraday Trans.*, **1997**, *93*, 1.
15. P. W. Fowler, *J. Chem. Soc., Faraday Trans.*, **1990**, *86*, 2073.
16. M. Yoshida, M. Fujita, P. W. Fowler, and E. C. Kirby, *J. Chem. Soc., Faraday Trans.*, **1997**, *93*, 1037.

17. D. J. Klein and H. Zhu, in: *From Chemical Topology to Three - Dimensional Geometry* (Ed. A. T. Balaban), Plenum Press, New York, 1997, pp. 297.
18. M. Deza, P. W. Fowler, M. Shtorgin, and K. Vietze, *J. Chem. Inf. Comput. Sci.*, **2000**, *40*, 1325.
19. B. de La VaissiÈre, P. W. Fowler, and M. Deza, *J. Chem. Inf. Comput. Sci.*, **2001**, *41*, 376.
20. P. W. Fowler and T. Pisanski, *J. Chem. Soc. Faraday Trans.*, **1994**, *90*, 2865.
21. T. Pisanski and M. Randić, in *Geometry at Work*, (Ed. C. A. Gorini) M. A. A. Notes, **2000**, ***53***, 174.
22. L. Euler, *Comment. Acad. Sci. I. Petropolitanae*, **1736**, *8*, 128.
23. L. Euler, *Novi Comment. Acad. Sci. I. Petropolitanae*, **1758**, *4*, 109.
24. F. Harary, *Graph Theory*, Addison-Wesley, Reading, MA, 1969.
25. V. Eberhard, *Zur Morphologie der Polyeder*, Leipzig,Teubner,1891.
26. P. W. Fowler, *Chem. Phys. Lett.*, **1986**, *131*, 444.
27. P. W. Fowler and J. I. Steer, *J. Chem. Soc.*, *Chem. Commun.*, **1987**, 1403.
28. P. W. Fowler and K. M. Rogers, *J. Chem. Soc.*, *Faraday Trans.*, **1998**, *94*, 1019.
29. P. W. Fowler, P. W. and K.M. Rogers, *J. Chem. Soc.*, *Faraday Trans.*, **1998**, *94*, 2509.
30. M. V. Diudea and P. E. John, *MATCH*, *Commun. Math. Comput. Chem.*, **2001**, *44*, 103.
31. M. V. Diudea, P. E. John, A. Graovac, M. Primorac, and T. Pisanski, *Croat. Chem. Acta*, 2003, *76*, 153.
32. A. E. Vizitiu, M. V. Diudea, S. Nikolić and D. Janežić, *J. Chem. Inf. Model.,* **2006**, *46*, 2574.
33. M. Goldberg, *Tôhoku Math. J.*, **1937**, *43*, 104.
34. M. V. Diudea, *Studia Univ.“Babes-Bolyai”*, **2003**, *48* (2), 3.
35. M. V. Diudea, *J. Chem. Inf. Model.,* **2005**, *45,* 1002.
36. R. B. King and M. V. Diudea, *J. Math. Chem.*, **2005**, 38 (4), 425.
37. R. B. King and M. V. Diudea, *J. Math. Chem.* **2006**, *39*, 597.
38. M. V. Diudea, in: M. V. Diudea, Ed., *Nanostructures-Novel Architecture*, NOVA, New York, **2005**, 203.

STUDIA UNIVERSITATIS BABEŞ-BOLYAI, CHEMIA, LIII, 2, 2008

NITRITE LINKAGE ISOMERISM IN BIOINORGANIC CHEMISTRY – A CASE FOR MECHANISTIC PROMISCUITY

RADU SILAGHI-DUMITRESCU, MATEI-MARIA UȚĂ[a]

ABSTRACT. Reduction of nitrite to nitric oxide is essential in certain living species, and has even been proposed to be an important secondary function of hemoglobin in humans. In vivo, nitrite reduction is accomplished by metalloenzymes, and involves direct metal-nitrite coordination at iron, copper, and possibly molybdenum. Using density functional (DFT) results, we have proposed that linkage (nitro/nitrito) isomerism is an essential part of the mechanism in one class of nitrite reductase enzymes. Here, DFT data is shown suggesting the generality of nitrite linkage isomerism in bioinorganic chemistry, and experimental data supporting this theory-driven proposal is briefly reviewed. The concept that nitrite reduction may be achieved by a given metalloprotein via two different mechanisms with the same product and comparable efficiencies is considered, as part of our recently-defined mechanistic promiscuity paradigm.

Keywords: *nitrite reductase, heme, hemoglobin, myoglobin, DFT, nitrate reductase, nitrite, nitric oxide*

INTRODUCTION

Under anaerobic conditions, many microorganisms can sustain growth by using nitrate as respiratory terminal electron acceptor [1]. Within these systems, nitrate and nitrite may be reduced to ammonia for the purpose of nitrogen assimilation (incorporation into organic matter, non-energy conserving) or dissimilation (using nitrate as respiratory electron acceptor, i.e., energy-conserving, but without incorporating the final reduced product into organic matter). Nitrate reduction to nitrite is catalyzed by molybdopterin-containing nitrate reductases. Subsequent reduction of nitrite is catalyzed by two types of nitrite reductases: those reducing nitrite to ammonia (cytochrome c nitrite reductase, siroheme-containing nitrite reductase) and those reducing nitrite to nitric oxide (copper-containing nitrite reductase, cytochrome cd_1 nitrite reductase) [2-4]. When produced by an NO-forming nitrite reductase, nitric oxide is further reduced to N_2O by nitric oxide reductases, which contain either cytochrome bd-or P450-type active sites [3].

---

[a] *Universitatea Babeş-Bolyai, Facultatea de Chimie şi Inginerie Chimică, Str. Kogălniceanu, Nr. 1, RO-400084 Cluj-Napoca,Romania, rsilaghi@chem.ubbcluj.ro*

In addition to the above-discussed nitrogen cycle, reduction of nitrite to nitric oxide has also recently been proposed to be an important secondary function of hemoglobin in humans, whereby the vasodilator molecule nitric oxide (of Nobel Prize fame) would be generated. The mechanisms whereby nitrite is reduced by hemes thus begin to entail increasing medical relevance [5].

RESULTS AND DISCUSSION

We have recently proposed that linkage nitro/nitrito isomerism is an essential part of the mechanism in the cases of copper and of heme d_1-containing nitrite reductases (NIR) [4,6]. Nitrite reduction by cytochrome cd_1 nitrite reductase (cd1NIR) had long been proposed to occur via N-coordination of nitrite to the d_1 heme of cd1NIR. Protonation of a nitrite oxygen atom within the ferrous-nitrite complex would lead to release of a water molecule, forming a weakly-bound complex, that subsequently decays via NO liberation.

Our group has however employed density functional theory (DFT) calculations to explore an alternative possibility, involving linkage isomerism of the nitrite at the NIR site [4,7]. Although the N- isomer (nitro) was found to be energetically favored over the O-nitrite (nitrito), even one single strong hydrogen bond may provide the energy required to put the two isomers on level terms. When hydrogen bonding existent at the cd1NIR active site was accounted for in the computational model, the O-nitrite isomer is found to spontaneously protonate and thus yield a ferric-hydroxo species, liberating nitric oxide. An O-nitrite ferrous cd1NIR complex appears to be an energetically-feasible intermediate for nitrite reduction. O-coordination would offer an advantage since the end-product of nitrite reduction would be a ferric-hydroxo/ water complex, rather than the more kinetically inert iron-nitrosyl complex implied by the N-nitrite mechanism.

A revised catalytic cycle for cd1NIR is thus illustrated in Scheme 2. This mechanism reconciles for the first time the cd1NIR chemistry with the puzzling fact that Fe(III)-NO is kinetically inert and hence cannot possibly be a part of the cd1NIR catalytic cycle.[4,7]

Reduction of nitrite to nitric oxide is also catalyzed by copper-containing NIR (Cu-NIR).[6,8] The proposed catalytic mechanism, illustrated in Scheme 2, has recently been confirmed by our own computational investigations.

Reduction of nitrite to nitric oxide is also catalyzed by copper-containing NIR (Cu-NIR).[6,8] The proposed catalytic mechanism, illustrated in Scheme 2, has recently been confirmed by our own computational investigations.

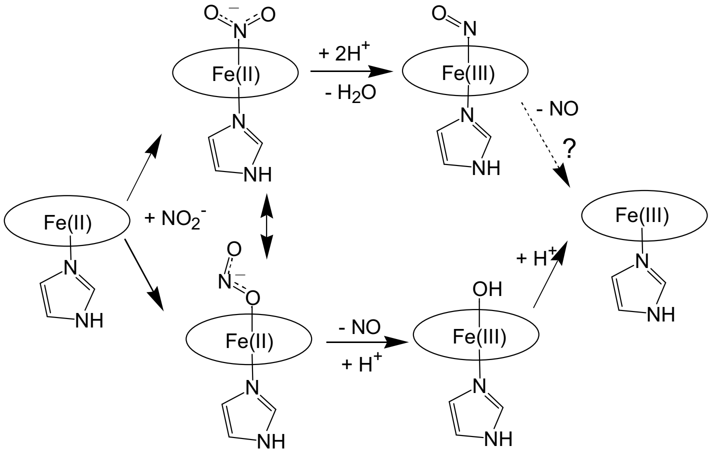

Scheme 1

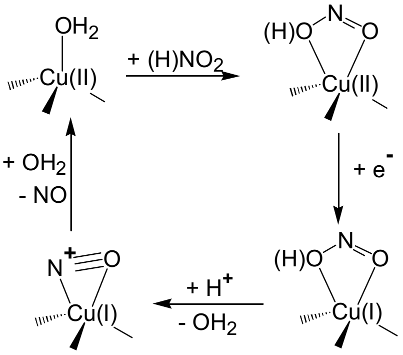

Scheme 2

Independent experimental work has also recently supported the concept that linkage isomerism has a profound influence on the products and mechanisms of catalytic reduction of nitrite by free hemes and related small complexes in solution [9,10]. Thus, the reactions of nitrate and nitrite with sodium dithionite in the presence of various metallo-macrocycles in aqueous alkaline solution lead to different products (nitrous oxide and ammonia, respectively). These differences were explained in terms of different structures of the intermediate complex between CoI phthalocyaninate and substrate, in which nitrite and nitrate were suggested to coordinate via nitrogen and oxygen, respectively. O-coordination of nitrite had also been proved for ruthenium and manganese porphyrinates [4,9].

Recent crystallographic work has for the first time established that nitrite coordinates to the iron in a hemoproteins, myoglobin, via the oxygen atom [11]. This result, supported by our unpublished EPR data, provides strong support for our linkage isomerism proposal in the case of cd1NIR.

Molybdenum-containing nitrate reductases from plants have more recently been proposed to be able to also reduce nitrite to nitric oxide [12]. Our unpublished DFT results support a role for linkage isomerism in this process.

CONCLUSIONS

Our current research interest is to explore nitrite linkage isomerism, attempting to establish trends and rules that govern this isomerism, with the ultimate aim of providing insight into inorganic catalysis as well as microbiological and medical issues related to nitrite metabolism. One of our working hypotheses is that nitrite reduction may be achieved by a given metalloprotein via two different mechanisms with the same product and comparable efficiencies; this would provide further support for our recently-defined mechanistic promiscuity paradigm, within the framework of which enzymes able to catalyze the same reaction via more than one mechanism may present an evolutionary advantage [13, 14].

ACKNOWLEDGMENTS

Funding from the Romanian Ministry for Education and Research (grant CEEx-ET 98/2006) is gratefully acknowledged. Profs. I. Silaghi-Dumitrescu and FD Irimie (BBU, Cluj-Napoca) and S. Makarov (ISUCT, Russia) are thanked for helpful discussions. Profs. C. Cooper, MT Wilson and D. Svistunenko (University of Essex) are thanked for helpful discussions and assistance with EPR experiments.

REFERENCES

1. D. J. Richardson,N. J. Watmough, *Curr. Opin. Chem. Biol.*, **1999**, *3*, 207.
2. O. Einsle, A. Messerschmidt, R. Huber, P. M. H. Kroneck,F. Neese, *J. Am. Chem. Soc.*, **2002**, *124*, 11737.
3. R. Silaghi-Dumitrescu, *Eur. J. Inorg. Chem.*, **2003**, 1048.
4. R. Silaghi-Dumitrescu, *Inorg. Chem.*, **2004**, *43*, 3715.
5. M. T. Gladwin, *Nat Chem Biol*, **2005**, *1*, 245.
6. R. Silaghi-Dumitrescu, *J Inorg Biochem*, **2006**, *100*, 396.
7. R. Silaghi-Dumitrescu, *Rev. Chim.*, **2004**, *55*, 496.

8. E. I. Tocheva, F. I. Rosell, A. G. Mauk,M. E. Murphy, *Science*, **2004**, *304*, 867.
9. E. V. Kudrik, S. V. Makarov, A. Zahl,R. van Eldik, *Inorg Chem*, **2005**, *44*, 6470.
10. E. V. Kudrik, S. V. Makarov, A. Zahi,R. van Eldik, *Inorg Chem*, **2003**, *42*, 618.
11. D. M. Copeland, A. S. Soares, A. H. West, G. B. Richter-Addo, *J Inorg Biochem*, **2006**, *100*, 1413.
12. A. F. Vanin, D. A. Svistunenko, V. D. Mikoyan, V. A. Serezhenkov, M. J. Fryer, N. R. Baker, C. E. Cooper, *J. Biol. Chem.*, **2004**, *279*, 24100.
13. R. Silaghi-Dumitrescu, I. Silaghi-Dumitrescu, *Chemtracts Inorg. Chem.*, **2005**, *18*, 595.
14. R. Silaghi-Dumitrescu,C. E. Cooper, *Dalton Trans.*, **2005**, 3477.

STUDIA UNIVERSITATIS BABEŞ-BOLYAI, CHEMIA, LIII, 2, 2008

LIGAND DOCKING AND SYSTEMATIC CONFORMATIONAL ANALYSIS IN LOOP MODIFIED PARSLEY PHENYLALANINE AMMONIA-LYASE STRUCTURE

AMALIA-LAURA SEFF[a], SAROLTA PILBÁK[b], LÁSZLÓ POPPE[b]

ABSTRACT. The phenylalanine ammonia-lyase (PAL) catalyzes the ammonia elimination from L-phenylalanine to (*E*)-cinnamic acid. A PAL model having more compact active center then the experimental *parsley* PAL (PDB code: 1W27) was constructed on the basis on different PAL and related enzyme structures (plant, bacterial and yeast) and their stability issues. In this PAL model (partial modified crystal structure) conformational analysis of the covalently bounded substrate to the MIO and ligand docking were performed to interpret experimental data.

Keywords: *phenylalanine ammonia-lyase, homology model, conformational analysis, docking*

INTRODUCTION

Phenylalanine ammonia-lyase (PAL EC 4.3.1.5) enzyme catalyzes the deamination from L-phenylalanine to (*E*)-cinnamic acid in the presence of an electrophilic prosthetic group: 5-methylene-3,5-dihydroimidazol-4-one (MIO) (Scheme 1) [1]. (*E*)-cinnamate is the precursor of a large number of plant metabolites, including lignin, coumarins, and flavonoids [2,3]. PAL is a key enzyme in the phenylpropanoid metabolism of plants. Polyethylene glycol-modified PAL can be considered for enzyme supplementation cure for the genetic disorder phenylketonuria [4].

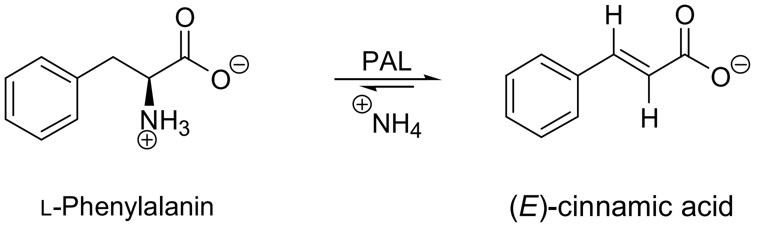

Scheme 1. Deamination of L-phenylalanine in the presence of PAL.

---

[a] *Faculty of Chemistry and Chemical Engineering, Babes-Bolyai University, Kogălniceanu Str. No. 1, RO-400084 Cluj-Napoca, Romania, samalia@chem.ubbcluj.ro*

[b] *Department of Organic Chemistry and Technology, Budapest University of Technology and Economics, H-1111 Budapest, Gellért tér 4, Hungary, poppe@mail.bme.hu*

Histidine ammonia-lyase (HAL) and tyrosine ammonia-lyase (TAL) enzymes are analogous of PAL. The structures and functions of these three ammonia-lyases are similar, because every of them contain the autocatalitically formed electrophilic MIO prosthetic group (Scheme 2) which is essential for the reaction [1].

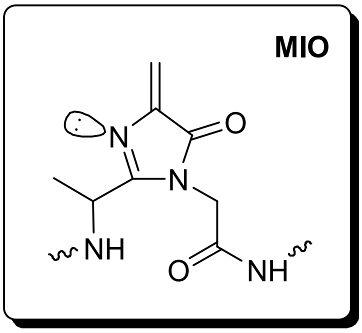

Scheme 2. The 5-methylene-3,5-dihydroimidazol-4-one (MIO) prosthetic group.

Since the catalytically essential Tyr110 residue containing loop region is missing from yeast PAL structure [5] and the parsley PAL (PDB code: 1W27) crystal structure [6] has an inactive conformation [7], we proposed to build a modified parsley PAL structure with a close active center, which can be adequate for mechanistic studies.

RESULTS AND DISCUSSION

Based on HAL structures [8], a modified parsely PAL structure was already built, which has a closer active center than the experimental PAL crystal structure [7]. Recently the TAL crystal structure was resolved [9], in which the essential Tyr-containing loop region has a compact conformation and therefore has a more closed active site. Based on the TAL (PDB code: 2O7B) structure, a new loop-modified PAL model was built. The tetramers of the parsley PAL crystal structure and the PAL model can be seen in Figure 1. A more detailed comparison of the two PAL active sites shows the Tyr110 residue in two different orientations. Tyr110 in our model points in the direction of MIO, whereas in the crystal structure was far from the active site (Figure 1).

Since the mechanism of the ammonia-lyase reactions involves a covalently bound intermediate (the substrate interacts with MIO due to it's N atom), systematical conformational search (CS) can be carried out within the rigid enzyme environment.

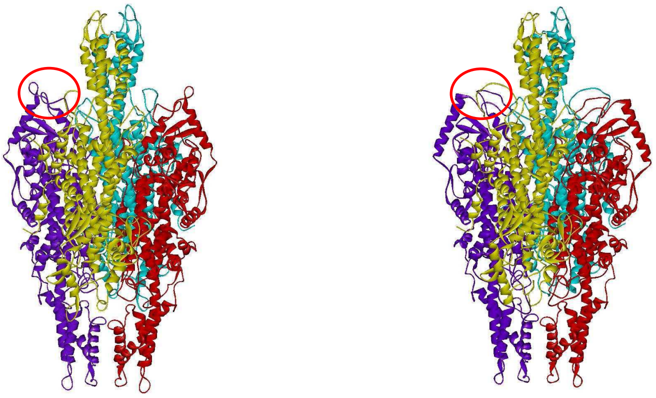

Parsley PAL tetramer (1W27) **Loop-modified PAL tetramer**

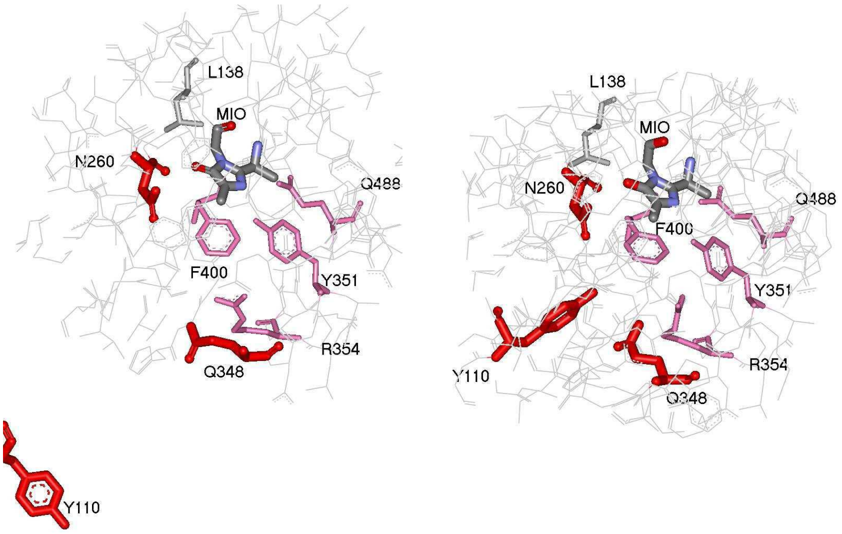
L138
MIO
N260
Q488
F400
Y351
R354
Q348
Y110
L138
MIO
N260
Q488
F400
Y351
Y110
R354
Q348

Figure 1. PAL tetramers and their active sites.

In the modified PAL crystal structure conformational analysis and ligand docking was performed. The two different analyses are in concordance, because the best *N*-MIO orientation obtained by CS has very similar orientation with the L-Phe in the docking result (Figure 2).

_N_-MIO conformational search

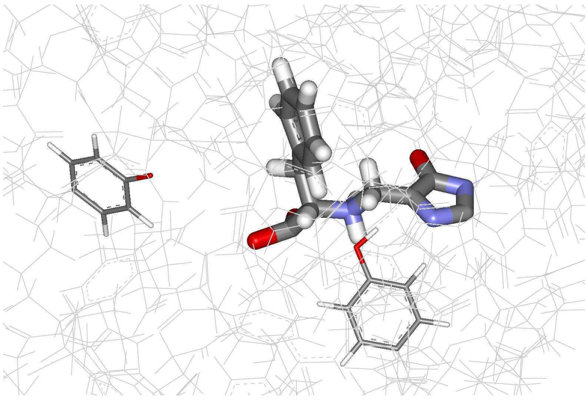

L-Phe docking

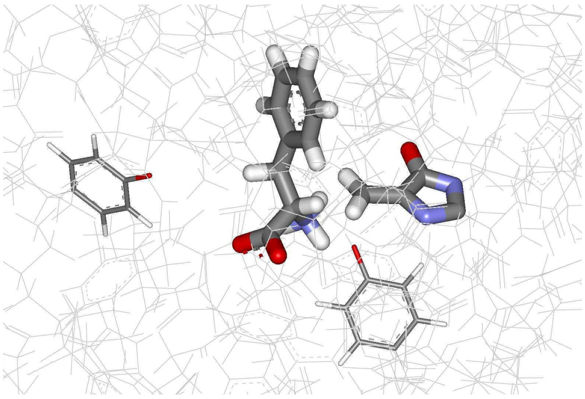

Figure 2. Results of conformational analysis and ligand docking within PAL.

EXPERIMENTAL SECTION

For our studies a 15 Å sphere around the MIO was cut out from the active site model. Next, by the HyperChem [10,11] standard procedure, hydrogen atoms were added to the amino acid residues of this raw active site model (the C- and N-termini at cutting were completed to neutral aldehyde and amino moieties). The MIO group was manually corrected [10]. For the *N*-MIO model three torsion angles of the ligand were varied during the CS [10]. The docking study was performed in ArgusLab.

CONCLUSIONS

Since the parsley PAL crystal structure has an inactive conformation, using homology modeling we built a TAL-like PAL structure, which has a completely closed active center. This gives us the possibility to study the reaction mechanism catalyzed by PAL enzyme.

The best docking poses are in accordance with the conformational analysis result of L-phenylalanine in the modified PAL structure.

ACKNOWLEDGMENTS

We thanks for the fellowship supported by SOCRATES/ERASMUS program.

REFERENCES

1. L. Poppe, J. Rétey, *Angewandte Chemie, International Edition English*, **2005**, *44*, 3668.
2. K. Hahlbrock, D. Scheel, *Annual Review of Plant Physiology and Plant Molecular Biology*, **1989**, *40*, 347.
3. C. Appert, E. Logemann, K. Hahlbrock, J. Schmid, N. Amrhein, *European Journal of Biochemistry*, **1994**, *225*, 491.
4. H.L. Levy, *Proceedings of the National Academy of Sciences of the United States of America*, **1999**, *96*, 1811.
5. J.C. Calabrese, D.B. Jordan, A. Boodhoo, S. Sariaslani, T. Vanneli, *Biochemistry*, **2004**, *43*, 11403.
6. H. Ritter, G.E. Schulz, *Plant Cell*, **2004**, *16*, 3426.
7. S. Pilbák, A. Tomin, J. Rétey, L. Poppe, *FEBS Journal*, **2006**, *273(5)*, 1004.
8. T.F. Schwede, J. Rétey, G.E. Schulz, *Biochemistry*, **1999**, *38*, 5355.
9. G.V. Louie, M.E. Bowman, M.C. Moffitt, T.J. Baiga, B.S. Moore, J.P. Noel, *Chemistry and Biology*, **2006**, *13*, 1327.
10. Hyperchem 7.5, Hypercube, Inc., **2003**.
11. Molfunction, Institute of Molecular Function, http://molfunction.com/

STUDIA UNIVERSITATIS BABEŞ-BOLYAI, CHEMIA, LIII, 2, 2008

SPECTRAL-SAR: OLD WINE IN NEW BOTTLE

MIHAI V. PUTZ[a,*] **and ANA-MARIA PUTZ (b. LACRĂMĂ)**[b]

ABSTRACT. With the aim providing an efficient and simple scheme of correlation between the chemical structures – on one hand – and the chemical properties or biological activities – on other hand – the available QSAR schemes are firstly grouped within classical, 3-dimensional, decisional, and orthogonal schemes while shortly reviewed their characteristics. Then, particular attention is paid on the recent orthogonal QSAR method, namely Spectral-SAR (S-SAR) algorithm, of which mathematical principles along its computational advantages are exposed. Application of S-SAR methodology is also given by modeling the mechanistic hierarchy of some xenobiotics ecotoxicology on the battery of *Protista*, *Monera*, and *Animalia* species kingdoms.

MOTIVATION

One of the main challenges in actual conceptual and computational chemistry stands the (quantum) transfer of the chemical interaction from local to global interaction in complex (biomolecular) systems. Although many attempts were advanced, based on reactivity and topological indices, the correlation analysis still remains to pay tribute to traditional QSAR (quantitative structure-activity relationship) statistical schemes. However, there is widely believed that while the chemical information is somehow iteratively carried from atoms to molecules to system a similar mathematical algorithm should follow the chemical bond and bonding from an intrinsic (structural or causal) to a manifested (observed or effector-receptor measured) levels [1].

Nevertheless, the superposition principle in quantum chemistry is here employed to the liner combination of intrinsic states assume to be orthogonal, i.e. carrying independent non-redundant information. In fact, the data from molecular real space (inherently with a degree of inter-correlation) has to be (at least) formally orthogonalized in an abstract space, see Figure 1, for a better approaching of bonding (correlation) analysis that has to be finally remapped in the real space however with the solved causality of actions. The present work reviews such an attempt.

---

[a] *Laboratory of Computational and Structural Physical Chemistry, Chemistry Department, West University of Timişoara, Pestalozzi Str. No.16, Timişoara, RO-300115, Romania; Tel: +40/256/592633, Fax: +40/256/592620*

[*] *E-mails: mv_putz@yahoo.com or mvputz@cbg.uvt.ro, Web: http://www.cbg.uvt.ro/mvputz*

[b] *Institute of Chemistry Timişoara of the Romanian Academy, 24 Mihai Viteazul Avenue, RO-300223, Timişoara, Romania*

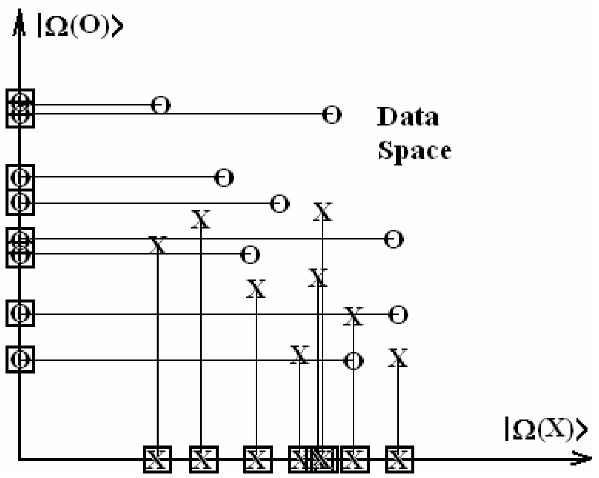

Figure 1. Generic mapping of data space containing the vectorial sets $\{|X\rangle, |O\rangle\}$ into orthogonal basis $\{|\Omega(X)\rangle, |\Omega(O)\rangle\}$ [1].

S-SAR METHODOLOGY

In that way, using the ideal condition of orthogonality of a QSAR correctional analysis the data space is considered as a vectorial one where the columns are treated like vectors, see Table I.

Table 1.

Spectral (vectorial) description of conventional SAR data [1-3].

Activity	*Structural predictor variables*					
$\|Y\rangle$	$\|X_0\rangle$	$\|X_1\rangle$	$\cdots$	$\|X_k\rangle$	$\cdots$	$\|X_M\rangle$
y_1	1	x_{11}	$\cdots$	x_{1k}	$\cdots$	x_{1M}
y_2	1	x_{21}	$\cdots$	x_{2k}	$\cdots$	x_{2M}
$\vdots$	$\vdots$	$\vdots$	$\vdots$	$\vdots$	$\vdots$	$\vdots$
y_N	1	x_{N1}	$\cdots$	x_{Nk}	$\cdots$	x_{NM}

Than, the vectorial space of data $\{|X_0\rangle, |X_1\rangle, ..., |X_k\rangle, ..., |X_M\rangle\}$ is transformed in an orthogonal one $\{|\Omega_0\rangle, |\Omega_1\rangle, ..., |\Omega_k\rangle, ..., |\Omega_M\rangle\}$ with the aid of iterative Gram-Schmidt procedure;

$$\left|\Omega_k\right\rangle = \left|X_k\right\rangle - \sum_{i=0}^{k-1} r_i^k \left|\Omega_i\right\rangle, \quad r_i^k = \frac{\left\langle X_k \middle| \Omega_i\right\rangle}{\left\langle \Omega_i \middle| \Omega_i\right\rangle}$$

with the help of scalar product rule for arbitrary N-dimensional vectors

$$\left|V\right\rangle = \left|v_1 \ldots v_N\right\rangle \text{ and } \left|W\right\rangle = \left|w_1 \ldots w_N\right\rangle:$$

$$\left\langle V \middle| W\right\rangle = \sum_{i=1}^{N} v_i w_i$$

Now the correlation equation in orthogonal space takes the form

$$\left|Y\right\rangle = \omega_0\left|\Omega_0\right\rangle + \omega_1\left|\Omega_1\right\rangle + \ldots + \omega_k\left|\Omega_k\right\rangle + \ldots + \omega_M\left|\Omega_M\right\rangle, \quad \omega_k = \frac{\left\langle \Omega_k \middle| Y\right\rangle}{\left\langle \Omega_k \middle| \Omega_k\right\rangle},$$

$$k = \overline{0, M}.$$

Since the come back in the real space is realized through the specific coordinate transformation

$$\begin{cases} \left|Y\right\rangle = \omega_0\left|\Omega_0\right\rangle + \omega_1\left|\Omega_1\right\rangle + \ldots + \omega_k\left|\Omega_k\right\rangle + \ldots + \omega_M\left|\Omega_M\right\rangle \\ \left|X_0\right\rangle = 1\cdot\left|\Omega_0\right\rangle + 0\cdot\left|\Omega_1\right\rangle + \ldots + 0\cdot\left|\Omega_k\right\rangle + \ldots + 0\cdot\left|\Omega_M\right\rangle \\ \left|X_1\right\rangle = r_0^1\left|\Omega_0\right\rangle + 1\cdot\left|\Omega_1\right\rangle + \ldots + 0\cdot\left|\Omega_k\right\rangle + \ldots + 0\cdot\left|\Omega_M\right\rangle \\ \ldots\ldots\ldots\ldots\ldots\ldots\ldots\ldots\ldots\ldots\ldots\ldots \\ \left|X_k\right\rangle = r_0^k\left|\Omega_0\right\rangle + r_1^k\left|\Omega_1\right\rangle + \ldots + 1\cdot\left|\Omega_k\right\rangle + \ldots + 0\cdot\left|\Omega_M\right\rangle \\ \ldots\ldots\ldots\ldots\ldots\ldots\ldots\ldots\ldots\ldots\ldots\ldots \\ \left|X_M\right\rangle = r_0^M\left|\Omega_0\right\rangle + r_1^M\left|\Omega_1\right\rangle + \ldots + r_k^M\left|\Omega_k\right\rangle + \ldots + 1\cdot\left|\Omega_M\right\rangle \end{cases}$$

that will generate the searched correlation equation, which results in the actual S-SAR equation [1-3]:

$$\begin{vmatrix} |Y\rangle & \omega_0 & \omega_1 & \cdots & \omega_k & \cdots & \omega_M \\ |X_0\rangle & 1 & 0 & \cdots & 0 & \cdots & 0 \\ |X_1\rangle & r_0^1 & 1 & \cdots & 0 & \cdots & 0 \\ \vdots & \vdots & \vdots & \vdots & & \vdots & \\ |X_k\rangle & r_0^k & r_1^k & \cdots & 1 & \cdots & 0 \\ \vdots & \vdots & \vdots & \vdots & & \vdots & \\ |X_M\rangle & r_0^M & r_1^M & \cdots & r_k^M & \cdots & 1 \end{vmatrix} = 0$$

thus providing the real activity-structural equation:

$$|Y\rangle = b_0|X_0\rangle + b_1|X_1\rangle + ... + b_k|X_k\rangle + ... + b_M|X_M\rangle$$

with the coefficients b_j, j=0, …, M, determined by expansion of above determinant along its first column.

Such algebraically approach of structure-activity correlation, allows the use of algebraically properties of the norm, here introduced as spectral norm,

$$\left\| |Y\rangle^{MEASURED/ \atop PREDICTED} \right\| = \sqrt{\sum_{i=1}^{N} (y_i^2)^{MEASURED/ \atop PREDICTED}}$$

together with new introduced correlation factor of algebraically type,

$$r_{S-SAR}^{ALGEBRAIC} = \frac{\left\| |Y\rangle^{P(REDICTED)} \right\|}{\left\| |Y\rangle^{M(EASURED)} \right\|}$$

Notably, the superiority of Spectral-SAR over traditional QSAR analysis was recently proved through the algebraic S-SAR correlation proposition [4]: in any vectorial analysis of Spectral-SAR type, considering the measuring and observed activity data as vectors $|Y^M\rangle$ and $|Y^P\rangle$ with the associate, while assuming the norm order

$$\left\| |Y^P\rangle \right\| \le \left\| |Y^M\rangle \right\|$$

the algebraic correlation factor will always exceed the standard QSAR statistical correlation factor , i.e. $r_{S-SAR}^{ALGEBRAIC} \ge r_{QSAR}^{STATISTIC}$, with

$$r_{QSAR}^{STATISTIC} = \sqrt{1-\frac{SR}{SQ}}\ ,\quad SR = \sum_{i=1}^{N}\left[y_i^M - y_i^P\right]^2\ ,$$
$$SQ = \sum_{i=1}^{N}\left[y_i^M - N^{-1}\sum_{i=1}^{N} y_i^M\right]^2 .$$

The study recommended the use of algebraically definition instead of the statistical one taking in consideration that the first has the physically meaning of “length of action” while replacing the standard dispersion definition. While the dispersion is a consequence of quality of fitting the vectorial norm of “length of action” simple describe the degree with which a certain model approaches the measured or manifested chemical-biological interaction.

S-SAR Ecotoxicology Applications

The Spectral-SAR methodology allows considering the spectral pathway of computed endpoints (activities) [1, 5]:

$$[A,B] = \sqrt{\left(\left\| Y^B \right\rangle\right\| - \left\| Y^A \right\rangle\right\|)^2 + \left(r_B^{STATISTIC/ ALGEBRAIC} - r_A^{STATISTIC/ ALGEBRAIC}\right)^2}$$

Moreover, the introduction of spectral way allows the formulation for the first time of a principle of optimization of pathways between the correlation models,

$$\delta[A,B] = 0;\quad A,B : ENDPOINTS$$

reflecting the optimisation of pathways between different endpoints of an open chemical-biological system. This principle says that from the all ways unifying the endpoints of a chemical-biologically system that pathway having the minimal length while finding the maximum possible combinations of the considered structural parameters is selected.

As such, the spectral scheme of the molecular mechanisms is obtained as a hierarchy of action influences of a series of chemicals on a certain species. Actually, the present Spectral-SAR model was tested for Hansch type regression by correlating the lipophylicity, the electronic polarizability and the total energy at the optimal configuration

$$A = b_0 + b_1\begin{pmatrix} hydrophobic \\ descriptor \end{pmatrix} + b_2\begin{pmatrix} electronic \\ descriptor \end{pmatrix} + b_3\begin{pmatrix} steric \\ descriptor \end{pmatrix}$$

with the ecotoxicity from different molecular levels and in various species.

At the unicellular level the ecotoxicity of the Tetrahymena pyriformis species was modeled employing the minimal spectral path procedure, i.e. ordering all the possible paths which connect endpoints from each mono-, bi- or tri-parametric category of models, see Figure 2.

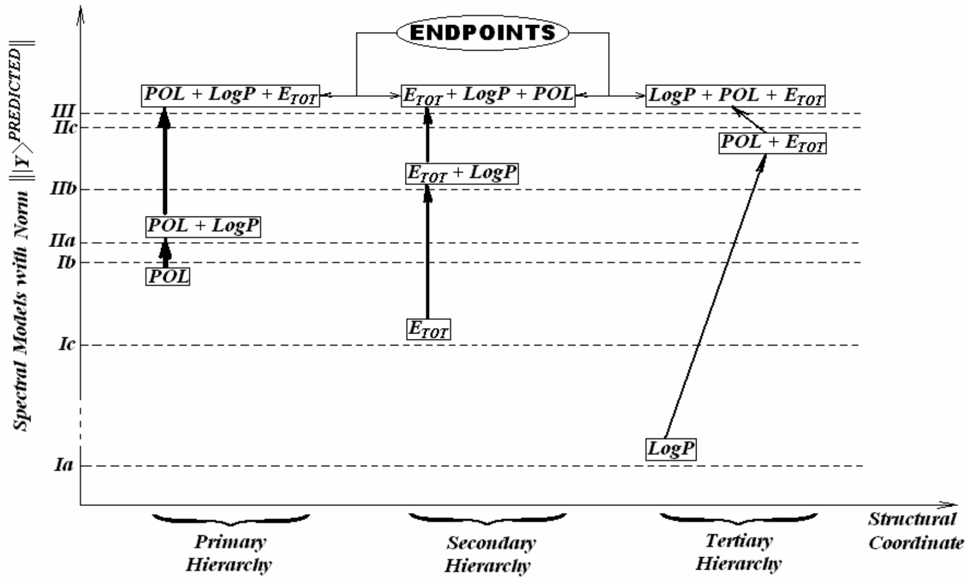
ENDPOINTS
POL + LogP + E_{TOT}
E_{TOT} + LogP + POL
LogP + POL + E_{TOT}
POL + E_{TOT}
E_{TOT} + LogP
POL + LogP
POL
E_{TOT}
LogP
Spectral Models with Norm $\| |Y\rangle^{PREDICTED} \|$
III
IIc
IIb
IIa
Ib
Ic
Ia
Primary Hierarchy
Secondary Hierarchy
Tertiary Hierarchy
Structural Coordinate

Figure 2. Spectral-structural models, designed through the rules of minimal spectral-SAR paths, emphasizing the primary, secondary and tertiary hierarchies forward the endpoints of the Tetrahymena pyriformis eco-toxicological activity [1].

Moreover, the logistic-spectral combined model was applied on ecotoxicological battery of organisms from selected species of Chlorella vulgaris, Vibrio fischeri and Pimephales promelas, giving the spectral representation of the molecular mechanisms intra- and interspecies based on the spectral paths and on their least principle. The resulted hierarchies (containing primary, secondary and tertiary molecular paths) are represented in the so called spectral scheme of interaction by the degree of thickness of the connecting lines, while the interference between the species toxicities are indicated by specific rectangular sign, for the primary hierarchies, and by circular sign for the secondary and tertiary hierarchies, see Figure 3.

Next, the ecotoxic-spectral-SAR model was accomplished for a series of ionic liquids activity measured on Vibrio fischeri species based on vectorial methodology generalization of structural data as the vectorial summation of cationic and anionic contributions in the resultant ionic liquid structure [6]

$$|Y_{AC}\rangle = |Y_C\rangle + |Y_A\rangle$$

while for the Daphnia magna action of the ionic liquids another scheme or anionic-cationic was employed in a generalized way [7]

$$\left|Y_{AC}\right\rangle^{0+} = \hat{O}_{S-SAR}\left|0+\right\rangle = \hat{O}_{S-SAR}\, f\left(\left\{\left|X_A\right\rangle\right\},\left\{\left|X_C\right\rangle\right\}\right)$$

with the specification of Hansch vectors:

$$f(LogP_A, LogP_C) \equiv LogP_{AC} = \log\left(e^{LogP_A} + e^{LogP_C}\right) \in \left\{\left|X_{1AC}\right\rangle\right\},$$

$$f(POL_A, POL_C) \equiv POL_{AC} = \left(POL_A^{1/3} + POL_C^{1/3}\right)^3 \in \left\{\left|X_{2AC}\right\rangle\right\} \ [\text{Å}^3],$$

$$f(E_A, E_C) \equiv E_{AC} = E_A + E_C - 627.71\frac{q_A q_C}{POL_{AC}^{1/3}} \in \left\{\left|X_{3AC}\right\rangle\right\} \ [\text{kcal/mol}].$$

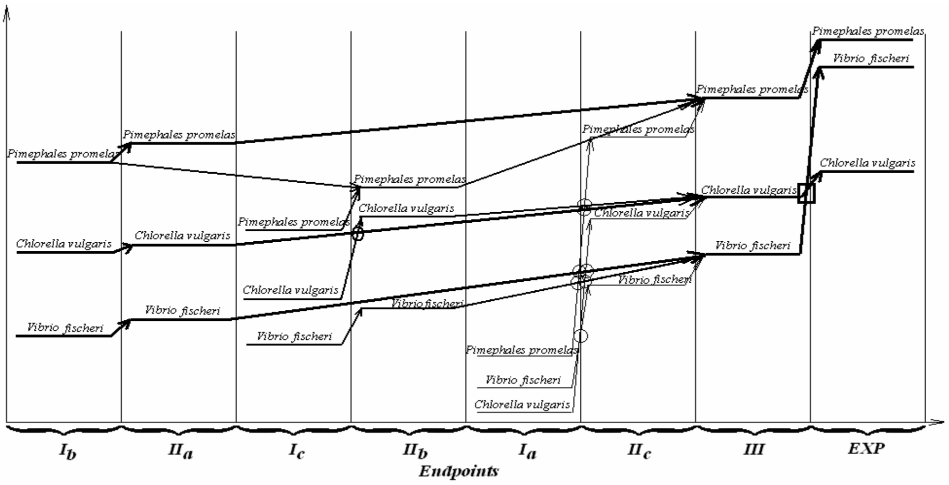

Figure 3. The spectral representation of the chemical-biological interaction paths across the S-SAR to experimental endpoints for the Chlorella vulgaris, Vibrio fischeri, and Pimephales promelas species, according with least path rule [5].

The obtained spectral hierarchies of the predicted activity relating different considered endpoints had provided the mechanistic scheme from which the cationic, anionic parts and ionic liquids in his integrity have different influence rules on the toxicity of the environment. There was concluded that while the tendencies of the cationic and anionic activities are complementary in a way they are not reduced in the ionic liquid summed up for approaching the total observed concentration in the spectral norm and correlation factor space, see Figure 4.

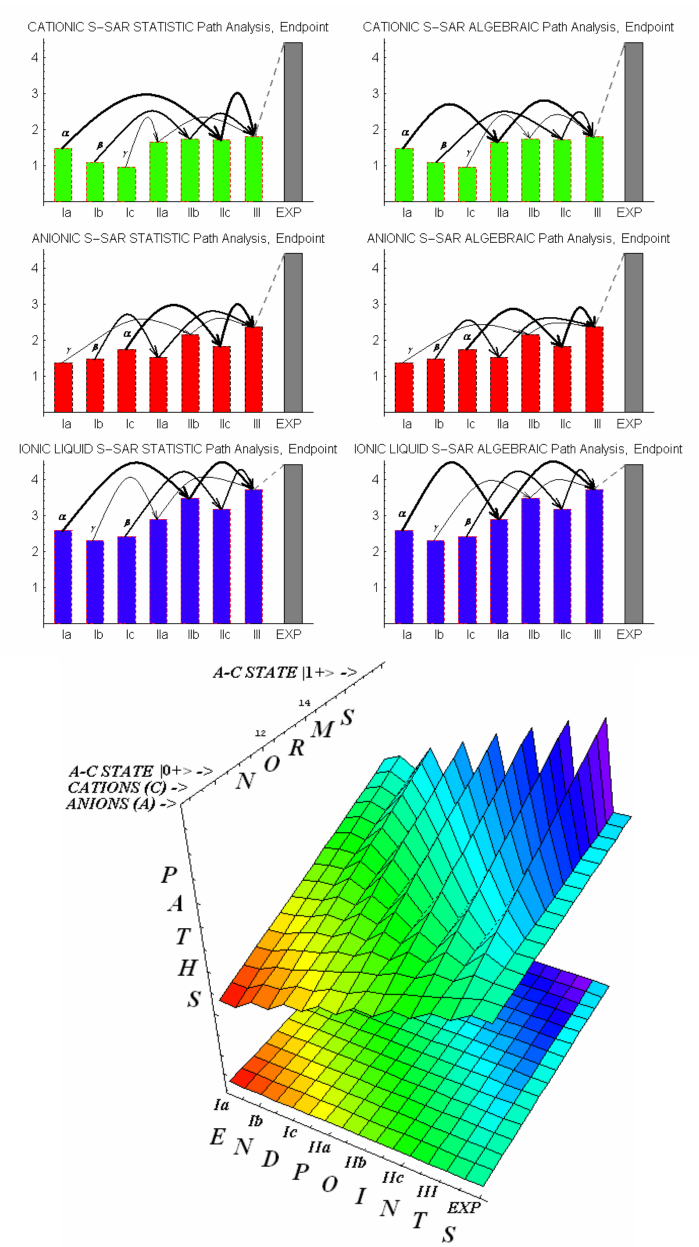

Figure 4. Spectral representation of the molecular hierarchical paths of the ecotoxicological action of specific ionic liquid series on Vibrio fischeri and Daphnia magna in left and right panels, respectively [6,7].

CONCLUSION

Through the structural and conceptual meaningful algorithm and the reliability in providing molecular paths of action in studied cases so far the present Spectral-SAR methodology opens the way in unifying the chemical-biological interactions and bonds in a 3D-dynamical (time dependency included) space.

REFERENCES

1. M.V. Putz, A.-M. Lacrămă, *Int. J. Molec. Sci.*, **2007**, *8*, 363.
2. M.V. Putz, *Annals of West University of Timişoara, Series of Chemistry*, **2006**, *15*, 159.
3. M.V. Putz, A.-M. Lacrămă, *Annals of West University of Timişoara, Series of Chemistry,* **2006**, *15*, 167.
4. M.V. Putz, C. Duda-Seiman, D. M. Duda-Seiman, A.M. Putz, *Int. J. Chem. Modeling*, **2008**, *1*, on line (https://www.novapublishers.com).
5. A.-M. Lacrămă, M.V. Putz, V. Ostafe, *Advances in Quantum Chemical Bonding Structures*, Mihai V. Putz (Ed.), Transworld Research Network, Kerala, India **2008**, ISBN: 978-81-7895-306-9, Chapter 16, pp. 389-419.
6. A.-M. Lacrămă, M.V. Putz, V. Ostafe, *Int. J. Molec. Sci.*, **2007**, *8*, 842.
7. A.-M. Lacrămă, M.V. Putz, V. Ostafe, *Research Letter in Ecology*, ID12813/5 pages, DOI: 10.1155/2007/12813, **2007**.

STUDIA UNIVERSITATIS BABEŞ-BOLYAI, CHEMIA, LIII, 2, 2008

GERMANIUM CLUSTER POLYHEDRA

IOAN SILAGHI-DUMITRESCU[a] **and BRUCE KING**[b]

ABSTRACT. Hybrid DFT B3LYP geometry optimizations on Ge_n^z (n=5 – 14), z= -6, -4, -2, 0, +2, +4,+6) have been undertaken in order to understand the structure of some post-transition metal cluster anions established experimentally by X-ray crystallography. Distortions from the expected geometries are interpreted in terms of hypo- or hyperelectronic counting of the skeletal electrons. Deviations from the Wade-Mingos rules noticed in several cases can be related to the use of the "external" electron pairs in the skeletal bonding.

Keywords: *germanium clusters, hypoelectronic clusters, hyperelectronic clusters, B3LYP DFT calculations.*

INTRODUCTION

Zintl phases discovered in 1930 [1-4] as the result of reaction of post-transition metals with sodium in liquid ammonia proved to be the beginning of an extremely fertile field of chemistry. Among other applications, such systems are considered as precursors for various nanomaterials. Zintl phases exhibit structural patterns (Table 1) varying from elemental structure shapes (a) to isolated tetrahedral units (b), oligomeric tetrahedral units (c), polymeric tetrahedral units (d), and highly condensed tetrahedral units (e). In all of these systems the covalently bound atoms share pairs of electrons in localized 2 center - 2 electron bonds. Unlike these species, a wealth of other types of structures (f) have been discovered where the number of skeletal electrons is different from that required by two centre bonds.

For the latter type of M_n systems the Wade-Mingos rules [18-21] state that if the number of skeletal electrons is 2n+2, the most spherical, closed deltahedral structure is expected. If however the number of skeletal electrons exceeds 2n+2 (hyperlectronic systems) the most favoured structures have non triangular faces (one for the so called *nido* clusters; two or one large open face for the so called "arachno" clusters). If the number of skeletal electrons is less then 2n+2 (hypoelectronic systems) several possibilities can occur to overcome this deficiency. Thus, the same polyhedron as in the case of 2n+2 electrons might be observed (but with some localized skeletal electrons), or a smaller

---

[a] *Universitatea Babes-Bolyai, Facultatea de Chimie si Inginerie Chimică, Str. Kogalniceanu, Nr. 1, RO-400084 Cluj-Napoca,Romania, isi@chem.ubbcluj.ro*

[b] *Department of Chemistry, University of Georgia, Athens, Georgia, rbking@chem.uga.edu*

polyhedron with some of the triangular faces capped by one atom, or 'flattening" of the 4-vertex atoms in such a way that the otherwise external electron pairs are drawn into the skeletal bonding.

Table 1.

Structural patterns encountered in Zintl phases.

	Phases	Reference
a	P_4 like Si_4^{4-}	5
	Si_4^{6-}	5
	Black phosphorus type $_\infty^2[As_3^{2-}]$, $_\infty^2[Sb_3^{2-}]$,	6,7
b	Isolated tetrahedral units: SiP_4^{8-}, $SiAs_4^{8-}$ GeP_4^{8-},$SnAs_4^{8-}$	8,9
c	Oligomeric tetrahedral units: $Si_2P_6^{10-}$, $Ge_2P_6^{10-}$, $Sn_2P_6^{10-}$	10-12
d	Polymeric tetrahedral units: $_\infty^1[SnP_3^{5-}]$, $_\infty^1[E(14)E(15)_2]^{2+}$ E(14)=Si,Ge,Sn, E(15)=P,As	13-14
e	Highly condensed tetrahedral frameworks: $^3_\infty[GaX_2^{3-}]$ X = P, As, Sb	15
f	Electron deficient structures Ga_{12}^{12-}, $Tl@Tl_{12}^{10-}$	16, 17

Several examples of main group metal clusters of the above types modeled by the electronically equivalent Ge_n clusters were discussed in the full presentation at MOLMOD 2007 held in Arcalia/RO [22]. Here we provide a short account of the main results.

RESULTS AND DISCUSSION

There are numerous experimentally realized examples of bipyramidal M_n clusters with 2n+2 skeletal electrons, which we have used to check the validity of the computational method chosen for this study. Table 2 lists some of the geometrical parameters for such clusters, along with the computed values of the isoelectronic Ge clusters. These data show that the overall shape of the cluster (expressed through the ratio of the eq-eq/ax-eq distance) is well reproduced by computing and, at least for the purpose of this investigation, the B3LYP method is sufficiently reliable.

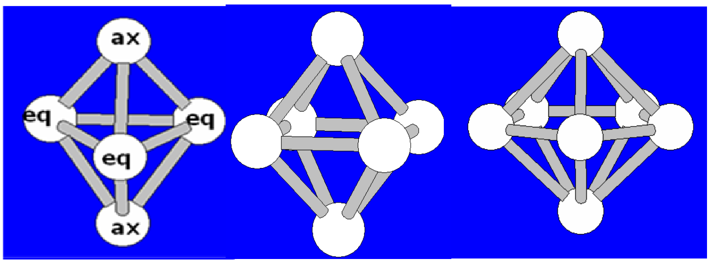

Figure 1. Three of the common bipyramidal structures encountered in cluster chemistry.

Table 2.

Relevant geometrical parameters for some bypiramidal clusters

Cluster	**eq–eq**	**eq–ax**	**ax…ax**	**eq–eq/ ax–eq**	**Ref.**
Ge_5^{2-}	2.818	2.577	3.997	1.09	23[e]
Ge_5^{2-}	2.68±0.02	2.49±0.03	3.90±0.02	1.08	24[c]
Sn_5^{2-}	3.238	3.002	4.70	1.08	25[e]
Pb_5^{2-}	3.095	2.877	4.49	1.08	25[e]
Bi_5^{3+}	3.326	3.013	4.646	1.10	26[e]
Tl_5^{7-}	3.280	3.214		1.02	27[e]
Tl_5^{7-}	3.32	3.15±0.01		1.05	28[e]
Ge_6^{2-}	2.687	2.687		1.00	23[c]
$[Ge_6\{Cr(CO)_5\}_6]^{2-}$	2.541	2.541		1.00	29[e]
Ge_7^{2-}				0.91	23[c]
$B_7Br_7^{2-}$				0.90	30[e]

[e]experimental data; [c]calculated data

Removal of two electrons from the Ge_n^{2-} clusters shown above leaves only 2n electrons for skeletal bonding. Various possibilities arise to compensate for these two missing electrons. One way is the flattening of the cluster so that two of the degree 4 vertices approach the center of the polyhedron with their otherwise external electron pairs thus becoming involved in the skeletal bonding (Figure 2). In the above Ge_n cases this deformation is observed as a shortening of the axial/axial Ge···Ge distances, in accord with the experimentally observed flattening of the isolobal and isoelectronic Tl_7^{7-} [31] or $Au_7(PPh_3)_7^+$ [32]

By decreasing the ax/ax distance, the population of the the external orbital bearing the lone pair of Ge in the Ge_n^{2-} cluster drops from values typically close to 2 down to 0.65 in Ge_5. Molecular orbitals of bipyramidal Ge_n^{2-} show that the HOMO is always Ge···Ge antibonding along the axial-axial direction, so the removal of two electrons from these orbitals increases the effective Ge···Ge bond orders thereby shortening these distances.

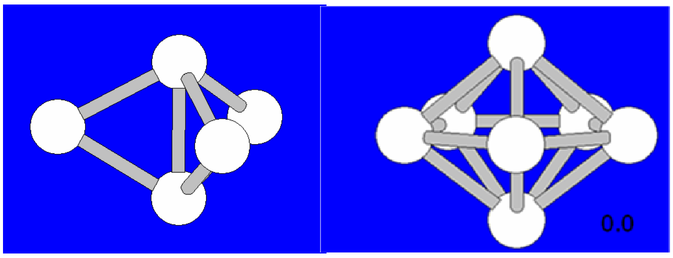

Figure 2. B3LYP/DFT optimized structures of Ge_5 and Ge_7

An interesting case occurs in Ge_8^{2-}, for which the global minimum is a tetracapped tetrahedron [33] rather than the bisdisphenoid expected from the Wade-Mingos rules (Figure 3). The other E_8^{2-} (E=Si, Ge, Sn) clusters also have a tetrahedral shape [34] in sharp contrast to the structure of the known **deltahedral borane** anion $B_8H_8^{2-}$ [35] and the isoelectronic neutral dicarbahexaborane $Me_2C_2B_6H_6$ [36], but in line with the **spherical (homo)aromatic** character assignable to the E_8^{2-} clusters [34].

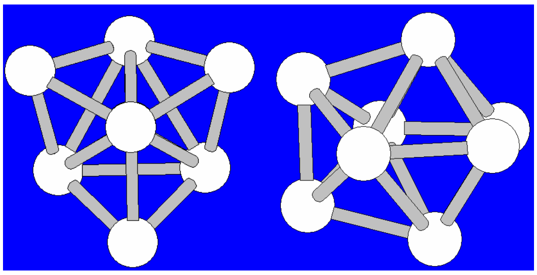

Figure 3. The lowest energy geometries of Ge_8^{2-}

Again, the occupation of the "lone pair" (LP) orbitals of the Ge atoms at the degree 6 vertices (forming the inner tetrahedron) drops to 0.69, as a result of a high degree of delocalization into the skeletal orbitals.

A similar violation of the Wade-Mingos rules has been noted for Ge_{11}^{2-}. Thus, $B_{11}H_{11}^{2-}$ is found both experimentally [37] and computationally [38] to have *a* C_{2v} edge-coalesced icosahedron structure whereas Ge_{11}^{2-} has a deformed pentacapped trigonal prism as its global minimum [38].

The eight- and eleven-vertex systems thus provide examples where lone pairs on Ge vertices versus hydrogen atoms on BH vertices make a significant difference in the relative stabilities of different polyhedral structures.

CONCLUSIONS

B3LYP/DFT calculations results on model $Ge_n^{z+/-}$ clusters focus on the influence of the external lone pairs of germanium atoms on the geometry of hypoelectronic and some of the electron precise clusters, providing thus rationale for the understanding the observed geometries of analogous systems.

EXPERIMENTAL SECTION

Hybrid B3LYP/6-311G* or Lanl2dz(d) calculations were carried out on Ge_n^z clusters (n=5-14) with z varying to cover a large variety of hypo- or hyperelectronic systems. The default fine grid in Gaussian 94 and Gaussian 98 [39,40] was used for integration. In all cases we started from the highest symmetry allowed by a particular arrangement/connectivity. The nature of the optimized structures were checked by vibrational analysis. When imaginary frequencies were found, the corresponding normal modes were followed in order to locate the genuine minima.

ACKNOWLEDGMENTS

We are indebted to the National Science Foundation for partial support of this work under Grant CHE-0209857. ISD thanks the CEEX Roumania (contract 4217-08-01) for financial support of the MOLMOD programme. We are also indebted to Prof. H. F. Schaefer, III, of the University of Georgia for providing computational facilities during several visits of ISD to the Center for Computational Quantum Chemistry, UGA .

REFERENCES

1. E. Zintl, J.Goubeau, W.Dullenkopf, *Z.Phys.Chem., Abt. A*, **1931**, *154*, 1.
2. E. Zintl, A.Harder, *Z.Phys.Chem., Abt. A*, **1931**, *154*, 47.
3. E. Zintl, W.Dullenkopf, *Z.Phys.Chem., Abt.B*, **1932**, *16*, 183.
4. E. Zintl, H.Kaiser, *Z.Anorg.Allg.Chem.,* **1933**, *211*, 113.
5. H. Schaefer, K.H. Janzon, A.Weiss, *Angew. Chem.Int.Ed. Engl.*, **1963**, *2*, 394.
6. K. Deller, B. Eisenmann, *Z.Naturforsch.*, **1976**, *31b*, 1550.
7. K. Deller, B. Eisenmann, *Z.Naturforsch.*, **1978**, *33b*, 676.
8. B. Eisenmann, H. Jordan, H. Schaefer, *Angew.Chem.Int.Ed.Engl.*,**1981**, *20*, 197.
9. B. Eisenmann, H. Jordan, H. Schaefer, *Mat. Bull.Res.*, **1982**, *17*, 95.
10. G. Gordier, G. Savelsberg, H. Schaefer, *Z.Naturforsch.*, **1982,** 37*b*, 975.
11. B. Eisenmann, M. Sommer, *Z.Naturforsch.*, **1985**, *40b*, 886.
12. B. Eisenmann, J. Klein, *Z.Krystallogr.*, **1991**,*196*, 213.
13. B. Eisenmann, J.Klein, *Z.Naturforsch.*, **1988**, *43b*, 1156.
14. B. Eisenmann, M. Sommer, *Z.Naturforsch.*, **1984**, *39b*, 736.
15. G. Cordier, E. Czech, M. Jakowski, H. Schäfer, *Rev. Chim. Miner.*, **1981**, *18*, 9.
16. W. Blase, G. Cordier, *Z. Naturforsch.*, **1989**, *44b*, 1479.
17. G. Cordier, V. Müller, *Z. Naturforsch.*, **1994**, *49b*, 935.
18. K. Wade. *Chem. Commun.* **1971**, 792.
19. K. Wade, *Adv. Inorg. Chem. Radiochem.* **1976**, *18*, 1.
20. D. M. P. Mingos, *Nature Phys. Sci.* **1972**, *99*, 236.

21. D. M. P. Mingos, *Acc. Chem. Res*. **1984**, *17*, 311.
22. I. Silaghi-Dumitrescu, Germanium Clusters-a Lesson to Learn, lecture presented at the 2nd "Molecular Modeling in Chemistry and Biochemistry" International Conference, Babes-Bolyai University, Arcalia Castle 5-8 July 2007.
23. R.B. King, I. Silaghi-Dumitrescu, A. Kun, *J.Chem.Soc. Dalton Trans*., **2002**, 3999.
24. J. Campbell and G. J. Schrobilgen, *Inorg. Chem.*, **1997**, *36*, 4078.
25. P. A. Edwards and J. D. Corbett, *Inorg. Chem.*, **1977**, *16*, 903.
26. S. Ulvenlund, K. Ståhl and L. Bengtsson-Kloo, *Inorg. Chem.*, **1996**, *35*, 223.
27. Z. Dong and J. D. Corbett, *Inorg. Chem.*, **1996**, *35*, 3107.
28. D. Huang and J. D. Corbett, *Inorg. Chem.*, **1999**, *38*, 316.
29. P. Kircher, G. Huttner, K. Heinze, G. Renner, *Angew. Chem., Int. Ed.*, **1998**, *37*, 1664.
30. A. Franken, H. Thomsen, W. Preetz, *Z. Naturforsch., Teil B*, **1996**, *51*, 744.
31. J. D. Corbett, D. Huang, Z. Dong, *Inorg. Chem.*, **1998**, *37*, 5881.
32. J. W. A. Van Der Velden, P. T. Beurskens, J. J. Bour, W. P. Bosman, J. H. Noordik, M. Kolenbrander, J. A. K. M. Buskes, *Inorg. Chem.*, **1984**, *23*, 146.
33. R.B.King, I. Silaghi-Dumitrescu. A. Lupan, *Dalton Trans*., **2005**, 1858.
34. Z. Chen, H. Jiao, A. Hirsch, P. R. von Schleyer, *Angew. Chem., Int. Ed.*, **2002**, *41*, 4309.
35. L. J. Guggenberger, *Inorg. Chem.*, **1969**, *8*, 2771.
36. H. Hart and W. N. Lipscomb, *Inorg. Chem.*, **1968**, **7**, 1070.
37. O. Volkov, W.Dirk, U. Englert, P. Paetzold, *Z. Anorg. Allg. Chem*., **1999**, *625*, 1193.
38. R.B. King, I. Silaghi-Dumitrescu, A. Lupan, *Inorg.Chem.*, **2005**, *44*, 7819.
39. Gaussian 98 (Revision A.11.3), M. J. Frisch, G. W. Trucks, H. B. Schlegel, G. E. Scuseria, M. A. Robb, J. R. Cheeseman, V. G. Zakrzewski, J. A. Montgomery, Jr., R. E. Stratmann, J. C. Burant, S. Dapprich, J. M. Millam, A. D. Daniels, K. N. Kudin, M. C. Strain, O. Farkas, J. Tomasi, V. Barone, M. Cossi, R. Cammi, B. Mennucci, C. Pomelli, C. Adamo, S. Clifford, J. Ochterski, G. A. Petersson, P. Y. Ayala, Q. Cui, K. Morokuma, P. Salvador, J. J. Dannenberg, D. K. Malick, A. D. Rabuck, K. Raghavachari, J. B. Foresman, J. Cioslowski, J. V. Ortiz, A. G. Baboul, B. B. Stefanov, G. Liu, A. Liashenko, P. Piskorz, I. Komaromi, R. Gomperts, R. L. Martin, D. J. Fox, T. Keith, M. A. Al-Laham, C. Y. Peng, A. Nanayakkara, M. Challacombe, P. M. W. Gill, B. Johnson, W. Chen, M. W. Wong, J. L. Andres, C. Gonzalez, M. Head-Gordon, E. S. Replogle, and J. A. Pople, Gaussian, Inc., Pittsburgh PA, **2002**.
40. Gaussian 94, Revision E.2, M. J. Frisch, G. W. Trucks, H. B. Schlegel, P. M. W. Gill, B. G. Johnson, M. A. Robb, J. R. Cheeseman, T. Keith, G. A. Petersson, J. A. Montgomery, K. Raghavachari, M. A. Al-Laham, V. G. Zakrzewski, J. V. Ortiz, J. B. Foresman, J. Cioslowski, B. B. Stefanov, A. Nanayakkara, M. Challacombe, C. Y. Peng, P. Y. Ayala, W. Chen, M. W. Wong, J. L. Andres, E. S. Replogle, R. Gomperts, R. L. Martin, D. J. Fox, J. S. Binkley, D. J. Defrees, J. Baker, J. P. Stewart, M. Head-Gordon, C. Gonzalez, and J. A. Pople, Gaussian, Inc., Pittsburgh PA, **1995**.